

TRAFFIC MONITORING SYSTEM USING IN-PAVEMENT FIBER BRAGG GRATING
SENSORS

A Dissertation
Submitted to the Graduate Faculty
of the
North Dakota State University
of Agriculture and Applied Science

By

Mu'ath Ahmad Al-Tarawneh

In Partial Fulfillment of the Requirements
for the Degree of
DOCTOR OF PHILOSOPHY

Major Department:
Civil and Environmental Engineering

May 2019

Fargo, North Dakota

North Dakota State University
Graduate School

Title

TRAFFIC MONITORING SYSTEM USING IN-PAVEMENT FIBER
BRAGG GRATING SENSORS

By

Mu'ath Ahmad Al-Tarawneh

The Supervisory Committee certifies that this *disquisition* complies with North Dakota
State University's regulations and meets the accepted standards for the degree of

DOCTOR OF PHILOSOPHY

SUPERVISORY COMMITTEE:

Dr. Ying Huang

Chair

Dr. Pan Lu

Dr. Amiy Varma

Dr. Raj Bridgelall

Dr. Zhili" Jerry" Gao

Approved:

06/25/2019

Date

Dr. David Steward

Department Chair

ABSTRACT

Recently, adding more lanes becomes less and less feasible, which is no longer an applicable solution for the traffic congestion problem due to the increment of vehicles. Using the existing infrastructure more efficiently with better traffic control and management is the realistic solution. An effective traffic management requires the use of monitoring technologies to extract traffic parameters that describe the characteristics of vehicles and their movement on the road. A three-dimension glass fiber-reinforced polymer packaged fiber Bragg grating sensor (3D GFRP-FBG) is introduced for the traffic monitoring system. The proposed sensor network was installed for validation at the Cold Weather Road Research Facility in Minnesota (MnROAD) facility of Minnesota Department of Transportation (MnDOT) in MN. A vehicle classification system based on the proposed sensor network has been validated. The vehicle classification system uses support vector machine (SVM), Neural Network (NN), and K-Nearest Neighbour (KNN) learning algorithms to classify vehicles into categories ranging from small vehicles to combination trucks. The field-testing results from real traffic show that the developed system can accurately estimate the vehicle classifications with 98.5 % of accuracy. Also, the proposed sensor network has been validated for low-speed and high-speed WIM measurements in flexible pavement. Field testing validated that the longitudinal component of the sensor has a measurement accuracy of 86.3% and 89.5% at 5 mph and 45 mph vehicle speed, respectively. A performed parametric study on the stability of the WIM system shows that the loading position is the most significant parameter affecting the WIM measurements accuracy compared to the vehicle speed and pavement temperature. Also, the system shows the capability to estimate the location of the loading position to enhance the system accuracy.

ACKNOWLEDGMENTS

Firstly, I would like to express my sincere gratitude to my advisor Dr. Ying Huang and co-advisor Dr. Pan Lu for the continuous support of my graduate study and related research, for their patience, motivation, and immense knowledge. Their guidance helped me in all the time of research and writing of this dissertation.

Besides my advisor, I would like to thank the rest of my thesis committee: Dr. Amiy Varma, Dr. Raj Bridgelall, and Dr. Zhili” Jerry” Gao, for their insightful comments and encouragement.

Furthermore, I would like to thank the engineers and staffs at MnROAD facility, MnDOT, for helping during the field-testing. Acknowledgments also give to the funding provided by the U.S. Department of Transportation under the agreement No.69A35517477108 through Mountain-Plains Consortium Project No. MPC-547, NSF ND EPSCoR DDA Project FAR0030957, and NSF Award No. CMMI-1750316. Also, I would like to thank the Civil and Environmental Engineering Department at NDSU.

Also, I would also like to thank my parents, two elder brothers, elder sister and my little sister. They are always supporting me and encouraging me with their best wishes. Finally, I would like to thank my family, Shaima’ Almbaidin, Leen, and Karim. They are always there cheering me up and stood beside me through the good times and bad.

DEDICATION

I dedicate this work to my mother (Amal Al-Tarawneh) soul who believed in me and taught me
the meaning of life.

TABLE OF CONTENTS

ABSTRACT.....	iii
ACKNOWLEDGMENTS	iv
DEDICATION.....	v
LIST OF TABLES.....	viii
LIST OF FIGURES	ix
1. INTRODUCTION	1
1.1. Research Background.....	1
1.2. Traffic Monitoring System.....	4
1.2.1. Weigh-in-Motion (WIM) technology.....	6
1.2.2. Existing WIM technology	7
1.2.3. Fiber optic sensor for traffic monitoring	9
1.3. Problem Statement and Significance of This Study.....	10
1.4. Objectives and Organization of This Dissertation	11
2. OPERATIONAL PRINCIPLE AND SENSOR NETWORK DESIGN.....	14
2.1. Sensor Design and Configuration	14
2.1.1. The operational principle of the FBG sensor	14
2.1.2. The 3D GFRP-FBG sensor geometric layout.....	15
2.2. Sensor Networking.....	16
2.2.1. Sensor network	16
2.2.2. Sensor installation and testing set up.....	18
2.3. Summary	20
3. VEHICLE CLASSIFICATION	21
3.1. Sensor Network	22
3.2. Vehicle Classification	23

3.2.1. Vehicle parameters derivation	23
3.2.2. Vehicle classification using SVM Machine Learning Classifier	26
3.3. Field Validation and Discussion	31
3.3.1. Vehicle parameters identification.....	31
3.3.2. Vehicle classification results	33
3.4. Vehicle Counts	37
3.5. Summary	39
4. WIM MEASUREMENTS IN FLEXIBLE PAVEMENT	40
4.1. 3D GFRP-FBG Sensor for WIM Measurements	40
4.2. Sensitivity Study	43
4.2.1. Sensor depth (z).....	44
4.2.2. Host material property (E).....	45
4.2.3. Load location (l)	47
4.3. Field Validation of a Case Study.....	49
4.3.1. Field testing setup.....	49
4.3.2. Field testing results.....	52
4.3.3. Field test results discussion	55
4.4. Summary	56
5. PARAMETRIC STUDY	57
5.1. Wheel Path	58
5.2. Vehicle Speed.....	69
5.3. Host Material Temperature	75
5.4. Traffic Monitoring System.....	78
6. CONCLUSION AND FUTURE WORKS	80
REFERENCES	82

LIST OF TABLES

<u>Table</u>		<u>Page</u>
1.	WIM sensor comparison [30-32]	9
2.	Vehicle classes description	27
3.	Proposed system measurements for the 5-axle truck	32
4.	Collected data.....	35
5.	OAO estimated vehicle classification.....	35
6.	OAA estimated vehicle classification.....	35
7.	NN estimated vehicle classification.....	36
8.	KNN estimated vehicle classification.....	37
9.	Material properties	52
10.	Estimated theoretic sensitivity (s) [unit: 10 ⁻⁶ nm/Kip]	54
11.	Field WIM measurements from the sensor at 5 mph and 45 mph	55
12.	Comparison of the WIM measurements with references.....	56
13.	KENLAYER model input for all loading positions.....	67
14.	WIM measurements error using the assumed loading positions	67
15.	WIM measurements error using the estimated loading positions.....	68
16.	KENLAYER model input at a different vehicle speed.....	71
17.	KENLAYER model input at different pavement temperature	77

LIST OF FIGURES

<u>Figure</u>	<u>Page</u>
1. Bridge collapse in France (1986) due to a traffic accident [3]	2
2. Truck rollover [3].....	3
3. Operational WIM station in the USA [24].....	6
4. Typical piezoelectric sensor [29]	7
5. Bending plate scale [27].....	8
6. Load cell [27].....	8
7. The operational principle of an FBG sensor [46]	14
8. Geometric design of the 3D GFRP-FBG sensor: (a) Photo of the 3D GFRP-FBG sensor, (b) Elevation view, and (c) Plan view (Unit: in.).....	16
9. Sensor networking (3D: three dimensions, 1D: one dimension, CL: center line)	18
10. MnROAD facility (a), the sensor installation scene (b), installation scene (c), and Cell 17 with embedded sensors after construction (d)	19
11. FHWA vehicle classification system [61]	22
12. Vehicle classification sensor networking (CL: center line).....	23
13. Operation principle to acquire the GFRP-FBG sensor's strain signal by convolution (a) and (b) the expected strain signal.....	24
14. Sensor responses for a passing two-axle vehicle	25
15. Diagram of binary SVM-OAA region boundaries on a basic problem [67].....	28
16. Diagram of SVM-OAO decision boundaries on a basic problem [67].....	29
17. Data fusion strategy scheme	30
18. MnROAD semi-truck (a), and sensor's response characteristic for five-axle truck (b)..	31
19. S1 sensor's responses for five-semi axle truck at 11.176 m/sec (25mph), 15.646 m/sec (35mph), and 18.776 (45mph)	33
20. Real traffic (a), and S1 sensor's response for 2 minutes of real traffic (b).....	34

21.	Sensor response for different vehicle class	38
22.	Sensor response for 250 seconds period	39
23.	Flexible pavement cross-section	42
24.	Sensor's WIM measurement sensitivity changes with sensor depth in longitudinal (L), transverse (T) and vertical (V) directions.....	45
25.	Sensor's WIM measurement sensitivity changes with pavement modulus of elasticity, E, in longitudinal (L), transverse (T) and vertical (V) directions	47
26.	Sensor's WIM measurement sensitivity changes with longitudinal location of the wheel in longitudinal (L), transverse (T) and vertical (V) directions.....	48
27.	Cell 17 flexible pavement cross section.....	50
28.	Master curve of Cell 17 HMA dynamic modulus test results.....	51
29.	The layout of MnROAD loading truck (a) and the truck dimension (b). (1'=1 ft., 1"=1 in.).....	53
30.	3D-2 longitudinal sensor's response at 5 mph and 45 mph vehicle speed	54
31.	Factors affecting the WIM system measurements accuracy.....	57
32.	Sensor network to determine the loading position.....	59
33.	Loading position scenarios	59
34.	Loading position estimation methodology.....	61
35.	Vehicle load distribution.....	62
36.	Loading positions.....	62
37.	3D-2 and 1D-3 sensors' responses for three runs using loading position L1	63
38.	3D-2 and 1D-3 sensors' responses for three runs using loading position L2	64
39.	3D-2 and 1D-3 sensors' responses for three runs using loading position L3	64
40.	3D-2 and 1D-3 sensors' responses for three runs using loading position L4	65
41.	Sensor's response changes with load location.....	66

42.	Weight measurement error for all loading positions (L1, L2, L3, and L4) using assumed loading positions (a) and using corrected loading positions (b)	69
43.	Dynamic modulus (E^*) changes with vehicle speed	70
44.	WIM sensitivity changes with vehicle speed.....	71
45.	3D-2 and 1D-3 sensors' response at 10 mph vehicle speed.....	72
46.	3D-2 and 1D-3 sensors' response at 20 mph vehicle speed.....	72
47.	3D-2 and 1D-3 sensors' response at 30 mph vehicle speed.....	73
48.	3D-2 and 1D-3 sensors' response at 40 mph vehicle speed.....	73
49.	3D-2 and 1D-3 sensors' response at 50 mph vehicle speed.....	74
50.	Weight measurements error at vehicle speed (10, 20, 30, 40, and 50) mph using assumed loading position (a) and using corrected loading position(b)	75
51.	Dynamic modulus changes with pavement temperature	76
52.	WIM measurements sensitivity changes with pavement temperature	76
53.	3D and 1D sensor's response at 17.1 °C pavement temperature.....	77
54.	Weight measurements error at pavement temperature (14.6, 17.1, and 19.9) °C using assumed loading position (Avg-B) and using corrected loading position (Avg-A).....	78
55.	Traffic monitoring system.....	79

1. INTRODUCTION

1.1. Research Background

Recently, adding more lanes becomes less and less feasible, which is no longer an applicable solution for the traffic congestion problem due to the increment of vehicles. Using the existing infrastructure more efficiently with better traffic control and management is the realistic solution. An effective traffic management requires the use of monitoring technologies to extract traffic parameters that describe the characteristics of vehicles and their movement on the road (i.e., vehicle velocity, traffic flow, travel time, vehicle density, vehicle dimension, length of the traffic jam, etc.). Knowing the vehicles type and weight have become very important for various traffic management applications, such as surveillance, access control, traffic demand planning, traffic congestion prevention, and accidents avoidance.

Weight data plays an important role in traffic planning, weight enforcement, and pavement condition assessment [1]. As a continuous increase of traffic loads, monitoring the overloaded trucks has become a more and more critical factor for the management of road networks, since the truck weight impacts significantly on the road maintenance costs and the safety of road users [2]. Overloading on roads would result in increasing deterioration level of the pavement which could lead to early pavement failure[3] since the damage of the pavement increases the 4th degree of power of exponential geometrics as the increase of vehicle weight [4]. Also, the overloaded truck increases the risk of accidents[5]. There are so many issues associated with the overloaded vehicles on our roads:

1. Damage to the road pavement and infrastructure: illegally overloaded vehicle causes severe damage to the road body and infrastructure. A study shows that a 10% increase in vehicle weight over the permitted weight will accelerate the pavement damage by

40% [6] since the overloaded trucks significantly increase pavement wear, cracking and rutting, which yields to early pavement failure. Also, another study shows that the combination of heavy load repetition is one of the major causes of longitudinal crack propagation [6]. Also, overloaded vehicles contribute to bridge fatigue damage. When trucks are heavy either carrying abnormal loads (e.g. cranes) or illegal overloads their effect on infrastructure (bridge, road, etc.) will be severe, which may yield to severely damage or even destroy the infrastructure. For example, In January 1986 in France, during a very cold period, a truck loaded with logs skidded on an icy section of the road entering the suspended bridge on the Loire river, hitting the bridge cable anchorage. This shock resulted in the fallout of the bridge following the failure of a cable anchorage, as shown in Figure 1[3].



Figure 1. Bridge collapse in France (1986) due to a traffic accident [3]

2. Traffic safety: The chance of involving an overloaded vehicle in and accidents is much higher than a legally loaded vehicle, also have much more severe consequences, and that is due to the face that overloaded vehicle generate large kinetic energy, which

results in greater damage and impact either to the road users or to the infrastructure. Also, there are so many consequences if the vehicle weight exceeds the permitted limit on the vehicle and the user safety, which can be concluded as follow: 1) Braking failure: a vehicle braking system failure due to the increasing weight. All breaking system components are designed for the maximum allowable weight, if the truck weight exceeds the allowable weight that will reduce the braking capacity and may yield to braking system failure; 2) Vehicle instability: an overloaded vehicle, especially truck is more likely to roll over or depart the road lane, as shown in Figure 2 comparing to legally loaded truck, because of the increased height at the center of gravity and more inertia of the vehicle bodies; 3) Tire overheat due to the overloads, which increases the risk of tire blow out; 4) Loss of maneuverability: a vehicle becomes underpowered due to the overloads, which results in loss of control of the vehicle on elevated road sections (up-hill and down-hill) [3].



Figure 2. Truck rollover [3]

3. Environmental impact: there are several environmental issues associated with the overloaded vehicle, such as noise and pollution.

4. Economic impact: a study shows that the maintenance cost of road calculated per one overloaded vehicle is 100% higher compared to the cost of the same legally loaded vehicle. Thus, a proper fee for an overloaded vehicle should be applied to recover the infrastructure damage cost [7, 8]. Also, overloaded vehicle violates the taxation rules, such as vehicle registration fees, axle taxes, and toll infrastructure.

Currently, law enforcement officer collects the suspected vehicles through visual assessment by direct the suspected vehicles into the static weighing station while the vehicles are at rest. Stationary weight scales together with weight stations are still the major weight control facilities worldwide. In general, there are three types of stationary weight scale [3]:

1. The fixed system: this system is permanently mounted in the pavement (concrete frames or platforms), and it used to measure gross weight and axle loads.
2. Semi-portable system: this system used permanent road installation (electrical wires, connections, etc.), but with a portable weight scale.
3. Portable system: this system uses weight scales which can be laid on pavement surface when it is needed (parking lot, ramps, any weighing area).

These stationary weight scales have some limitations; staff is needed for both selecting the vehicle from the traffic flow and perform static weighing. They are time-consuming with waiting time from 10 to 30 minutes, limited spaces for trucks to pass by [9], potentials for missing overloaded trucks [5], and accident hazards [10]. Thus, to overcome these limitations, Weight-In-Motion (WIM) technology has become popular for weight measurements for road networks.

1.2. Traffic Monitoring System

Increasing traffic congestion in the United States is a growing problem in many countries. The 2014 Urban Mobility Report [11] estimates the total annual cost of congestion for the 471

U.S. urban areas in 2013 \$153 billion of wasted time and fuel and an extra 6.8 billion hours of travel and 3.1 billion gallons of fuel consumed. Also, monitoring regional and national truck fleet has become very important for various applications, such as better understanding of freight pattern, fuel consumption, road safety, and emissions. Thus, monitoring of traffic is very important. Traffic monitoring is performed to collect data that describes the use and performance of the roadway system [12]. A system to monitor traffic on the road requires two significant components, including sensor networks either on the sides of the roads or inside the pavement and framework to analyze the acquired data. For roadside sensors, there are various technologies available, including infrared sensors, microwave doppler or radar, passive acoustic sensors, and video image detection [13,14]. These roadside sensors are easy to install and repair, however, their performances are significantly affected by atmospheric particulates, surrounding environments, and weather conditions [13,15–18], which are also subjected to damages from harsh weather conditions. To avoid the limitations of the roadside sensors, there are a variety of in-pavement electrical and magnetic sensing technologies including inductive loops [13,18,19], magnetic sensors [20,21], pneumatic tubes [13], and in-pavement WIM sensing technologies. The inductive loop sensors are very cheap but reported to have a high failure rate associated with installation in poor road surfaces and the use of substandard installation procedures. The magnetic sensors have a better success rate but smaller detection zones and large magnetic field interference from the environments. The pneumatic tubes have bigger detection area but were reported to have significant interferences from pavement temperature and vehicle speed and may produce inaccurate axle counting when truck and bus volumes are very high. In general, most of the electrical and magnetic sensors showed a significant dependence on surrounding environments

and had limitations for long-term use in the field, which would not last the design life of the pavements [13].

1.2.1. Weigh-in-Motion (WIM) technology

The concept of WIM was introduced more than 50 years ago [22]. Currently, there are more than 1,000 operational WIM stations on the US highway system [23] as shown in Figure 3.

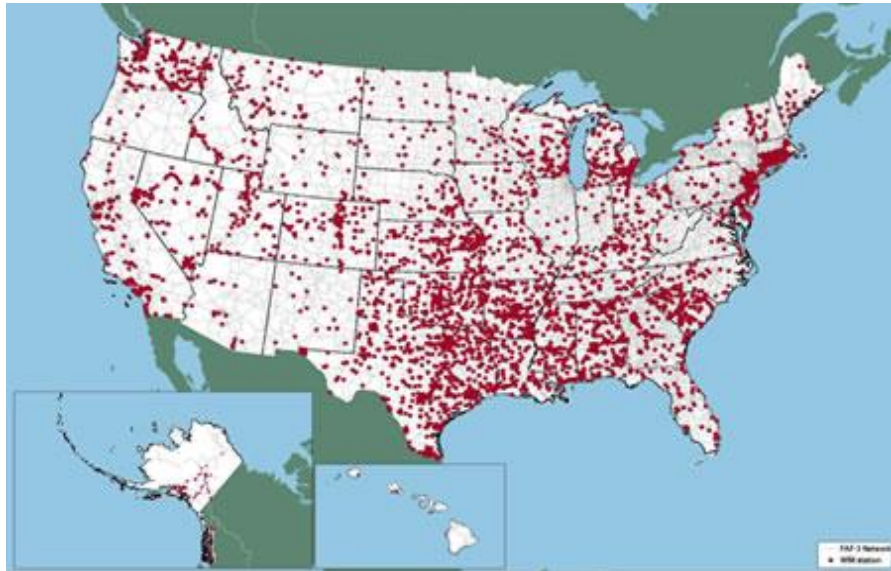


Figure 3. Operational WIM station in the USA [24]

A WIM system is defined as a system that used to measure the dynamic axle load of a moving vehicle to estimate the static axle weight. An effective WIM system includes at least three components: a network of in-pavement sensors, a facility for data acquisition, and an algorithm or framework for WIM data extraction. In general, The WIM system can be categorized into two types based on the operating vehicle speed: low-speed weigh-in-motion (LS-WIM) for passing the speed of up to 25mph, and high-speed weigh-in-motion (HS-WIM) for the vehicle passing speed up to 80mph. Both appeared in late of the 1960s [25]. Agencies usually apply LS-WIM sensors in combination with stationary weight scales for weight enforcement purposes and pavement design and maintenance. With the growing demand to collect real traffic data and weight information,

especially after the introduction of weigh-station bypass programs, there is a greater need for an HS-WIM system. The WIM can produce a useful traffic data such as wheel weight, axle weight, gross vehicle weight, speed, wheelbase, vehicle type (via axle arrangement), lane and direction of travel, travel time, sequential vehicle identification number, and equivalent single-axle loads (ESALs), according to American Society for Testing and Materials (ASTM) [26].

1.2.2. Existing WIM technology

There are several of in-pavement sensing technologies which can be used for traffic monitoring, including piezoelectric sensor, bending plates, load cells, and fiber optic sensors [27]:

- 1) Piezoelectric sensor: The most common WIM device. The sensor is embedded in the pavement, and when a load is applied to the piezoelectric material, an electrical charge is produced. The vehicle weight could be measured by analyzing the produced electrical charges. The WIM system based on the Piezoelectric sensors can provide gross vehicle weights with a measurement accuracy of 15% for 95% of the measured trucks. Figure 4 shows the typical piezoelectric sensor [28].

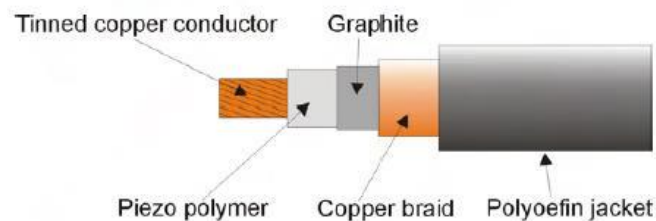


Figure 4. Typical piezoelectric sensor [29]

- 2) Bending plate scale: The bending plate scale consists of two steel platforms that are (2 ft. x 6 ft.) in size, placed close to each other in an appropriate distance to cover a 12 ft. as shown in Figure 5. The plates are instrumented with strain gages, which installed at critical points in order to measure the generated strain due to the applied tire load. The

WIM system based on the bending plate sensors can provide gross vehicle weights with a measurement accuracy of 10% for 95% of the measured trucks [28].



Figure 5. Bending plate scale [27]

- 3) Load cell: This device consists of two 6 ft. x 6 ft. weighing platforms, placed close to each other in an appropriate distance to cover a 12 ft, as shown in Figure 6. A single hydraulic load cell is installed at the center of each platform to measure the tire load induced forces that are then transformed into tire loads. The WIM system based on the load cell can provide gross vehicle weights with a measurement accuracy of 6% for 95%. [28].

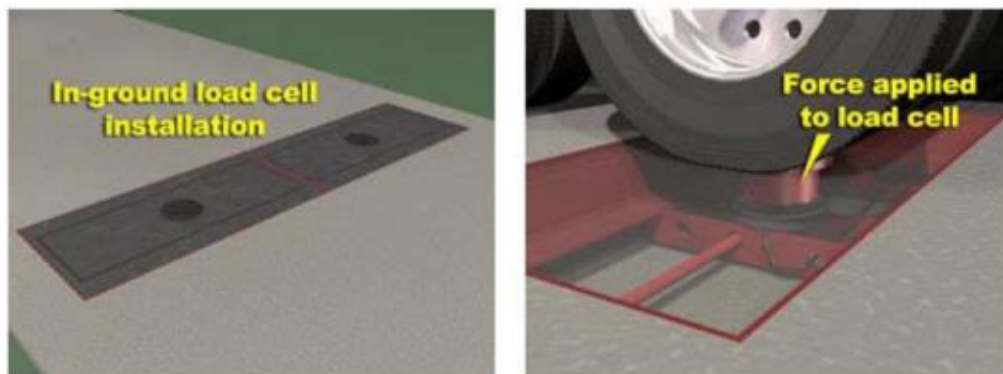


Figure 6. Load cell [27]

These sensors (piezoelectric sensor, bending plate scale, and load cell) generally show inversely proportional cost and accuracy characteristics. Table 1 shows that the electrical sensors (piezoelectric sensor, bending plate, and load cell) have a relatively high cost and short design life

with moderate accuracy. Also, bending plate and load cell sensors require extensive civil engineering work for installation, which may yield to some damage to the host material. In general, all the electrical sensors have a high level of electromagnetic interference (EMI) and their performance significantly affected by the surrounding environmental factors

Table 1. WIM sensor comparison [30-32]

	Piezoelectric sensor	Bending plate	Single load cell
Annual life cycle cost	Low (\$ 5,000)	Medium (\$ 6,000)	High (\$ 8,000)
Accuracy	+/- 15%	+/- 10%	+/-6%
Sensitivity	High	Medium	Low
Expected life	4 years	6 years	12 years

1.2.3. Fiber optic sensor for traffic monitoring

In recent years, optic fiber sensors have been used for traffic engineering application due to their unique advantages of small size, lightweight, high sensitivity, immunity to electrical magnetic interference (EMI), ability to embedded in hostile environment, low cost of less \$1,000, easy installation, and long design life [33, 34]. These advantages may provide a potential solution for reliable long-term in-pavement traffic monitoring sensors. Currently, Fiber Bragg Grating (FBG) sensor are commonly used for civil engineering applications and has been widely accepted in field applications in order to measure loads, strain, and temperature [30, 31]. The FBG was firstly formatted in an optical fiber in 1978 in Canada [35]. A single FBG sensor could potentially provide a lot of traffic parameters, such as vehicle weight, vehicle speed, vehicle type, pavement fatigue, and temperature. All these advantages can extend the system's durability [36]. Hence, it can be a potential solution for the traffic monitoring system, and it has been tested for such application as follow:

- 1) Wang et al. [37] stated that the experimental results showed good repeatability for WIM measurement based on FBG sensor installed on steel plates.
- 2) Moyo et al. [38] stated that the assessment of traffic loading on bridges could be achieved by using the FBG sensor;
- 3) Berardis et al. [39] indicated that a traffic monitoring system based on FBG sensors is good for high-speed road vehicle and high load resolution;
- 4) Cass et al. [40] showed that FBG sensors could be used to monitor traffic factors on roads such as vehicle speed and its weight;
- 5) Udd et al. [41] showed that a single FBG sensor is effective to monitor vehicle speed, vehicle type, and vehicle weight by installing the FBG sensor on a bridge;
- 6) Mimbela et al. [42] indicated that a fiber optic sensor in WIM system applications show considerable promise for meeting both traffic monitoring needs and as part of the national and local ITS architecture plans

However, the installation process may easily damage the sensor because the construction of FBG contains silica material. Thus, the packaging is necessary for FBGs in any field applications. Glass-fiber-reinforced polymer (GFRP) material provides durable and reliable packaging which has become widely accepted for use in civil engineering applications [43]. Hence, researchers used the GFRP material to package a three-dimension (3D) FBG sensor to improve its ruggedness. In this study, we will investigate a GFRP packaged FBG sensor for the traffic monitoring system to extract traffic parameters, including weight, speed, class, and vehicle count.

1.3. Problem Statement and Significance of This Study

From the above literature review, extracting traffic parameters, which describe the characteristics of vehicles and their movement on the road (i.e. traffic volume, vehicle speed,

vehicle weight, and vehicle class) have become very important for various traffic management applications, such as surveillance, access control, traffic demand planning, traffic congestion prevention and accidents avoidance. Thus, it is necessary to have a traffic monitoring system which can collect such data and analyze them.

To construct a traffic monitoring system, sensing units either on the sides of the roads or inside the pavement are needed. For roadside sensors, including infrared sensors, microwave doppler or radar, passive acoustic sensors, and video image detection, their performances are significantly affected by atmospheric particulates, surrounding environments, and weather conditions. To avoid the limitations of the roadside sensors, there are a variety of in-pavement electrical Weigh-In-Motion (WIM) sensing technologies, including Piezoelectric sensor, bending plate scale, load cell, and fiber optic sensor. The unique advantages of the FBG (small size, light weight, high sensitivity, low cost, and high accuracy) over the electrical sensors make the FBG sensor commonly used for civil engineering applications. In the other hand, the FBG sensor is very weak without packaging.

From the above literature review, it is obvious that there is a need to develop a robust approach for a long-term traffic monitoring system. FBG sensor is a potential candidate, but with a single FBG which is made up of glass fiber, it is not robust enough to survive during the harsh paving process of the pavement construction and the hostile environment (temperature, moisture, etc).

1.4. Objectives and Organization of This Dissertation

In this study, the main objective is to develop an effective GFRP packaged FBG sensor for a robust and cost-effective long-term traffic monitoring system. To achieve this objective, this study identifies four specific tasks which can be summarized as follow:

- 1) Construct a traffic monitoring sensor network using GFRP-FBG sensors;
- 2) Develop the GFRP-FBG sensor for an effective vehicle classification:
 - a) Use the proposed system for speed and wheelbase estimation.
 - b) Develop the vehicle classification using SVM Machine Learning Classifier.
 - c) Validate the proposed system field testing of case study
- 3) Develop the GFRP-FBG sensor for LS-WIM and HS-WIM measurements inside flexible pavement in order to estimate the vehicle wheel weight:
 - a) Develop the weight transfer function theoretically;
 - b) Perform a sensitivity study of the sensor on several key parameters, such as sensor depth, load coordination, and host material property on the sensitivity of the GFRP-FBG sensor for the WIM measurements;
 - c) Validate the developed sensor for WIM measurement through field testing of a case study.
- 4) Investigate the stability of the proposed system in the flexible pavement with different influencing factors:
 - a) Investigate the effect of the loading position on the weight measurements, and propose a new methodology to determine the loading position;
 - b) Study the effect of the vehicle speed on the system accuracy for the weight measurements;
 - c) Investigate the effect of the pavement temperature on weight measurement accuracy;
 - d) Propose a traffic monitoring system based on the GFRP-FBG sensors for a two-lane highway with a typical lane width of 12 ft.

This dissertation is thus organized as follows: in Chapter 1, an introduction of traffic monitoring system and a detail literature review are provided; in Chapter 2, the operational principle of the FBG sensor, the geometric design of the GFRP-FBG WIM sensor are introduced, along with the sensor network establishment ; in Chapter 3, the traffic monitoring system using in-pavement GFRP-FBG sensor is introduced for vehicle classification, and a part of this chapter is delivered from the following journal paper (Vehicle classification system using in-pavement fiber Bragg grating sensors. *IEEE Sensors Journal*. 2018 Feb 7;18(7):2807-15.), and from the following conferences paper (In-pavement fiber Bragg grating sensors for high-speed weigh-in-motion measurements. In *Sensors and Smart Structures Technologies for Civil, Mechanical, and Aerospace Systems 2017* 2017 Apr 12 (Vol. 10168, p. 101681Y). International Society for Optics and Photonics), and (Road vehicle classification using machine learning techniques. In *Sensors and Smart Structures Technologies for Civil, Mechanical, and Aerospace Systems 2019* 2019 Mar 27 (Vol. 10970, p. 109700O). International Society for Optics and Photonics); in Chapter 4, the GFRP-FBG sensor is introduced for LS-WIM, and HS-WIM measurements in flexible pavements, including sensitivity study of controlling factors on the sensitivity of the sensor and field testing of case study is performed for validation, and a part of this chapter is delivered from the following conference paper (In-pavement fiber Bragg grating sensors for high-speed weigh-in-motion measurements. In *Sensors and Smart Structures Technologies for Civil, Mechanical, and Aerospace Systems 2017* 2017 Apr 12 (Vol. 10168, p. 101681Y). International Society for Optics and Photonics); in Chapter 5, the stability of the WIM system will be introduced; and in Chapter 6, conclusion and future work have been presented based on the findings from this study.

2. OPERATIONAL PRINCIPLE AND SENSOR NETWORK DESIGN

Glass Fiber Reinforced Polymer Fiber Bragg Grating (GFRP-FBG) sensor has been selected to be used for traffic monitoring in flexible pavements. In this chapter, the operational principle of the FBG sensor, the geometric design, and the sensor network based on the GFRP-FBG sensor are introduced in detail.

2.1. Sensor Design and Configuration

2.1.1. The operational principle of the FBG sensor

The formation of FBG in optical fiber was first demonstrated by Hill et al. in 1978 at the Canadian Communications Research Centre (CRC), Ottawa, Ont., Canada,[44]. An FBG is made by launching intense Argon-ion laser radiation into a Germania-doped fiber [44]. The Bragg wavelength is formed due to reflected light from the periodic refraction change, as shown in Figure 7, which can be described as [45]:

$$\lambda = 2n\Lambda \quad (1)$$

where, n is the effective index of refraction and Λ is the grating periodicity of the FBG.

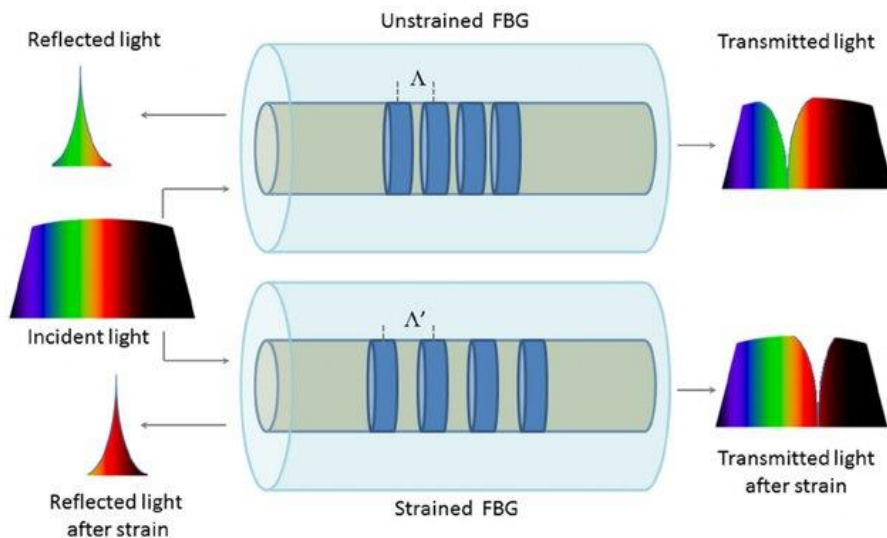


Figure 7. The operational principle of an FBG sensor [46]

Due to temperature and strain dependence of the grating period, Λ , the Bragg wavelength changes as a function of temperature, T_e , and strain, ε . The general expression of the strain–temperature relationship for the FBG strain sensor and temperature compensation sensor can be described as [45]:

$$\frac{\Delta\lambda_1}{\lambda_1} = \frac{\Delta\lambda_\varepsilon}{\lambda_\varepsilon} + \frac{\Delta\lambda_{T_e}}{\lambda_{T_e}} = (1 - P_e)\varepsilon + (\alpha + \gamma)\Delta T_e \quad (2)$$

$$\frac{\Delta\lambda_2}{\lambda_2} = \frac{\Delta\lambda_{T_e}}{\lambda_{T_e}} = (\alpha + \gamma)\Delta T_e \quad (3)$$

where, α , γ , and P_e are thermal expansion coefficient, thermal-optic coefficient, and the optical elasticity coefficient of the optic fiber, respectively. λ_1 is the Bragg wavelength from the FBG, which experiencing strain and temperature changes, and λ_2 is the Bragg wavelength from the FBG temperature compensation sensor.

The temperature and strain may also affect the fiber’s elasto-optic and thermos optic properties. However, due to the fact that the testing period is in a short duration for one WIM measurement, the changes of elasto-optic and thermo-optic effect on strain and temperature are neglected. Thus, the strain of the sensor can be calculated by subtracting Equation 2 from Equation 3 [45]:

$$\varepsilon = \frac{1}{(1 - P_e)} \left(\frac{\Delta\lambda_1}{\lambda_1} - \frac{\Delta\lambda_2}{\lambda_2} \right) \quad (4)$$

2.1.2. The 3D GFRP-FBG sensor geometric layout

Since the FBG sensor is made by glass fiber and not robust for direct embedment in pavements, this study uses GFRP material to package the FBG sensors. The 3D GFRP-FBG sensor previously developed by the authors’ research group [45, 47, 48] has been selected to be a sensor unit.

Figure 8 (a~c) shows the geometric design for the 3D GFRP-FBG sensor with three components: one in vertical, one in longitudinal, and one in transverse directions. The short-gauged component of the sensor intends to detect the vertical strain while the long-gauged component used to detect the longitudinal and transverse strains. The FBG used in this study has a length of 2.5mm (0.1 in.) and diameter of $\sim 250\mu\text{m}$, and it was inserted in the middle of each component (both in diameter and length) of the 3D sensor. All the three components of the 3D GFRP-FBG sensor share the same diameter of 5mm (0.2 in.). The horizontal and transverse components have a length of 4.06 cm (1.6 in.), and the vertical component has a length of 3.05 cm (1.2 in.). The center wavelength of the longitudinal, transverse, and vertical gauges in the 3-D GFRP-FBG sensor are 1544.292 nm, 1549.493 nm, and 1539.581 nm, respectively. Also, the GFRP-FBG sensor has a strain sensitivity of $7.937 \times 10^{-7} \text{ nm}/\mu\epsilon$, which is $(1-P_e)$ term in Equation 4.

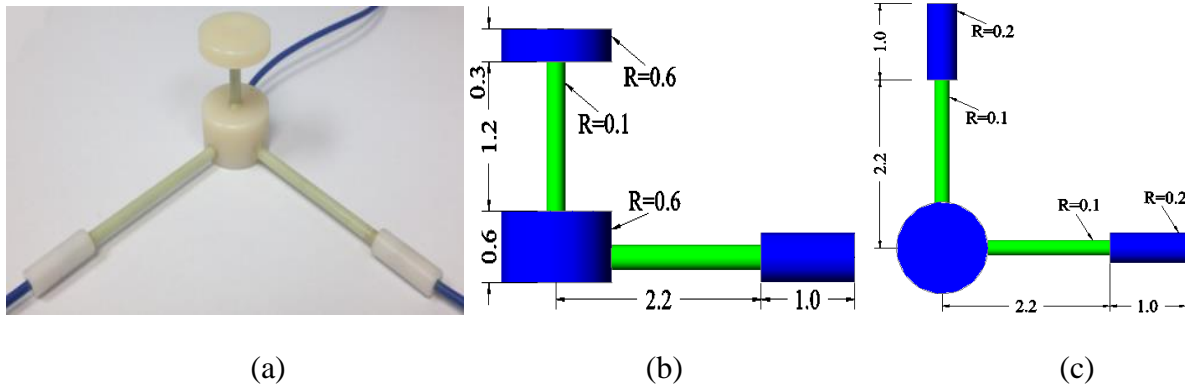


Figure 8. Geometric design of the 3D GFRP-FBG sensor: (a) Photo of the 3D GFRP-FBG sensor, (b) Elevation view, and (c) Plan view (Unit: in.)

2.2. Sensor Networking

2.2.1. Sensor network

An effective traffic monitoring system requires a sensor network with multiple sensors inside the pavements for data collections. To ensure the detection of all vehicle's axles and

estimation the wheelbase and other traffic parameters, accurate vehicle speed estimation is the key. Therefore, a sensor network with an acceptable speed estimation error will be needed to construct an effective traffic monitoring system. Numbers, locations, and distances between sensors are the major factors influencing the accuracy of a sensor network. To effectively estimate the vehicle speed and the wheelbase, it requires a minimum of two sensors in the network, which need to be installed under the vehicle wheel path for maximum measurement sensitivity. The optimized distance between the two in-pavement sensors in the network for vehicle detection and classification usually falls between 7 ft. and 20 ft. [49, 50]. Also, the variation caused by the inaccurate installation of the sensors (D is the distance between parallel sensors) will cause some systematic error in speed estimation. To minimize this systematic installation error, the distance between sensors should be large to get maximum speed estimation accuracy [51].

In this study, a sensor network is formed using the minimum numbers of sensors required, which is two 3D GFRP-FBG sensors. A distance of 16 ft. in between the two sensors is used which is in between 7 ft. and 20 ft. as suggested by the literature. The sensors are installed under the wheel path to be more accurate for vehicle passing measurements. In addition to the two 3D GFRP-FBG sensors, to eliminate the temperature effects using Equation 4, one temperature compensation FBG sensor was installed 2.42 ft. away from the 3D-2 sensor inside Pavement Cell 17 to monitoring the pavement temperature variances, which has a temperature sensitivity of 13 pm/°C. Since there are no tree shades in Cell 17, only one temperature compensation sensor was installed. Also, to study the multiple tires and dynamic effects in the future, a 1D GFRP-FBG sensor was installed on the side of Sensor 3D-2 as shown in Figure 9.

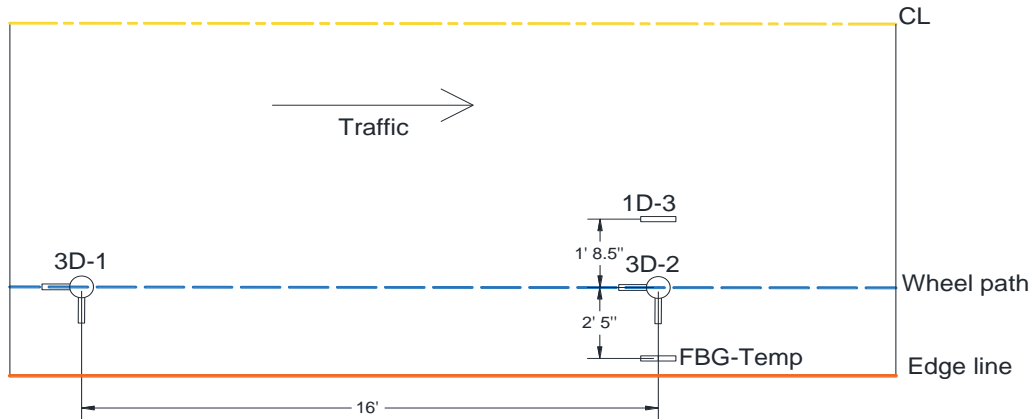
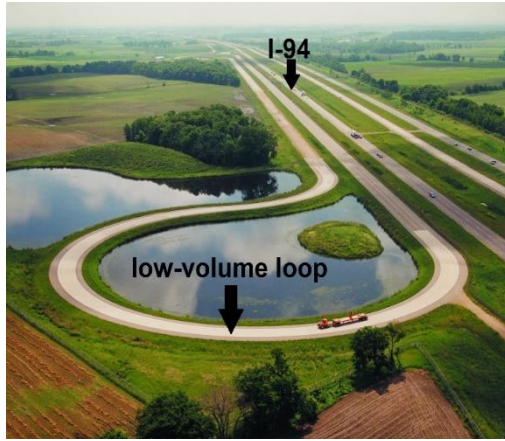


Figure 9. Sensor networking (3D: three dimensions, 1D: one dimension, CL: center line)

2.2.2. Sensor installation and testing set up

In order to validate the developed traffic monitoring system based on the 3D GFRP-FBG sensor network, field testing was performed at the Cold Weather Road Research Facility in Minnesota (MnROAD) facility of Minnesota Department of Transportation (MnDOT) in MN, U.S.A. MnROAD consists of two unique roadways: a two-lane low-volume loop that is loaded with a 5-axle 40 tons (80 kips) semi-truck and a section of interstate I-94 “mainline” that contains two westbound lanes with live traffic. The proposed sensor network in Figure 9 was installed inside the Pavement Cell 17, one section of interstate I-94 at MnROAD, which belongs to the I-94 “mainline” westbound lanes as shown in Figure 10 (a). The 3D GFRP-FBG sensors were installed beneath the wheel path on the asphalt pavement as shown in Figure 10 (b), and in Figure 10 (c and d) for the photo of the sensor installation scene and Cell 17 after construction.



(a)



(b)



(c)



(d)

Figure 10. MnROAD facility (a), the sensor installation scene (b), installation scene (c), and Cell 17 with embedded sensors after construction (d)

The two 3D GFRP-FBG sensors were installed under the expected wheel path that was 9 ft. from the centerline of the road on the right lane of the road, the distance of 9 ft. was chosen to guarantee the detection of all rolling vehicles on the right lane, also since the vehicles may not pass over the top of the sensor, the sensitivity study in the previous study shows that the 3D GFRP-FBG longitudinal and vertical components still effectively detect the vehicle's tire within 6 inches range from the sensor installation location . The distance between the two sensors was 16 ft. as required by the sensor networking in Figure 9. Installing the vertical component in the asphalt layer puts the component at failure risk due to the compaction during the paving process.

Therefore, the longitudinal components of the 3D sensors were installed at the bottom of the road asphalt layer (5 in. under the road surface) and the vertical components of 3D sensors were installed in the base layer and sealed with asphalt sealing to fix it in the desired location (1.6 in. beneath the base layer).

After the installation of the sensor network, the three components of the sensors in the network together with a temperature compensation FBG sensor were connected to an FBG integrator with 5 KHz sampling rate. The FBG integrator was further connected to a personal computer to record the data.

2.3. Summary

In this Chapter, the operational principle of the FBG sensor and the geometric design of GFRP-FBG sensor are described. FBG sensor is used as a strain sensor. The generated Bragg wavelength changes of the FBG sensor depends on the strains on the grating, and the strains can be directly related to the applied load (vehicle weight) on the pavement. In this study, GFRP is used as packaged material for FBG sensor. The GFRP packaged FBG WIM sensor contains three components, one in the longitudinal direction, one in transverse, and one in the vertical direction, and it has a strain sensitivity of $7.937 \times 10^{-7} \text{ nm}/\mu\epsilon$.

Also, an effective sensor network using multiple sensors inside the pavements was introduced for data collections. In order to validate the developed traffic monitoring system based on the 3D GFRP-FBG sensor network, field testing was performed at the Cold Weather Road Research Facility in Minnesota (MnROAD) facility of Minnesota Department of Transportation (MnDOT) in MN.

3. VEHICLE CLASSIFICATION

In 1980, Federal Highway Administration (FHWA) of United States developed a vehicle classification system [52], which divide vehicle type into 13 categories depending on the number of axles and the wheelbase as shown in Figure 11. Establishing a fixed threshold for classifying a vehicle is difficult, with the overlapping between vehicles pattern in the system, which needs a pattern recognition technique to distinguish between different vehicle categories. Pattern recognition is a scientific discipline whose aim is to classify the objects into a lot of categories or classes [53]. Pattern recognition algorithms have been widely used for numerous applications, such as medicine, weather forecasting, stock exchange forecast, geology, and vehicle classification. Many effective pattern recognition methods have been used for vehicle classification in the literature, including vision-based preceding vehicle recognition method [54], inductive classifying artificial network (ICAN) [55], fuzzy inference system [56, 57], the probabilistic neural network method [58,59], and the support vector machines (SVM) learning method [60]. The SVM machine learning classifier predicts the output from the given input developed in Russia in the sixties, and reported as a well-founded technique in statistical learning theory [60]. In this Chapter, a vehicle classification system was developed based on a sensor network from GFRP packaged FBG sensors supported by the SVM machine learning method to extract the vehicle classification information. The developed vehicle classification system was validated by real field traffic.

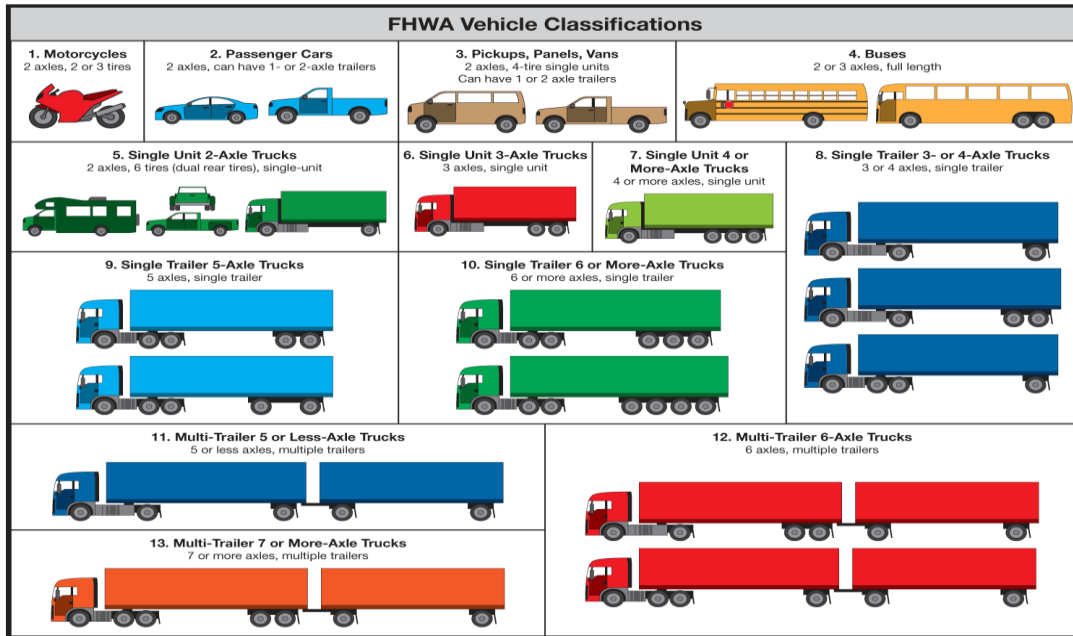


Figure 11. FHWA vehicle classification system [61]

3.1. Sensor Network

In this study, a sensor network of two 3D sensors (3D-1 and 3D-2) was used in the field testing, as indicated in Chapter 2, as shown in Figure 12. The performed sensitivity study in the previous study [62] shows that the longitudinal component has the largest weigh-in-motion (WIM) measurements sensitivity among the other components, followed by the vertical component. Thus, to validate that both longitudinal and vertical components of the 3D sensors work well for vehicle classification, one longitudinal component of sensor 3D-1 (S1) and one vertical component of sensor 3D-2 (S2) were used to feed the vehicle classifier for classification.

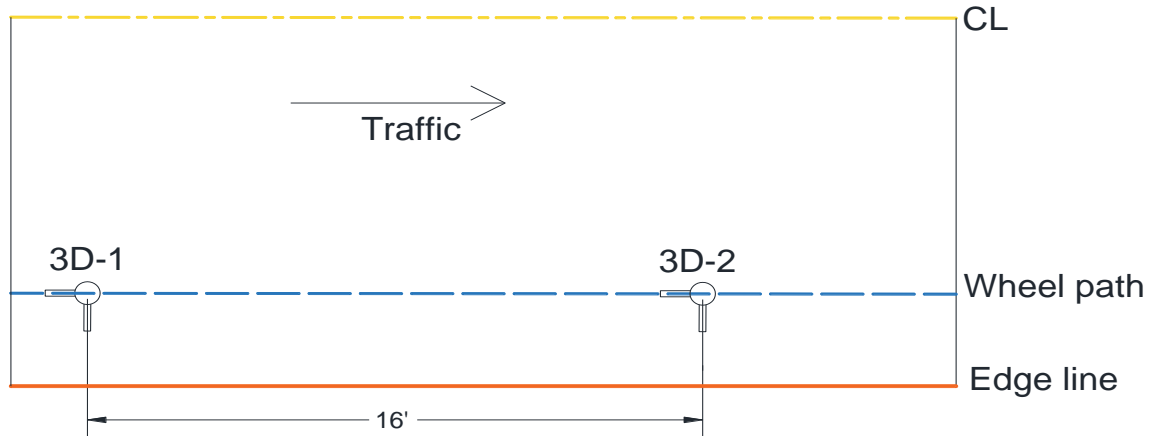


Figure 12. Vehicle classification sensor networking (CL: center line)

3.2. Vehicle Classification

3.2.1. Vehicle parameters derivation

To classify passing vehicles, an embedded network of sensors inside the pavements will need to sense the number of axles, the axle spaces, and the speed of a passing vehicle. When a vehicle tire passes over the road, the pavement produces strain signals, and so does the embedded 3D GFRP-FBG sensor. From Equation 4, it can be seen that the strain changes on an FBG sensor will produce corresponding Bragg wavelength changes which can be recorded and analyzed to recover the strain information inside the pavements. Thus, all the vehicle classification information, including the number of axles and axle spaces are closely related to the induced strains inside the pavements by the passing vehicles.

The strain signal inside the pavement is formed from the convolution of the load from the tire contact area and the sensitivity function of the embedded sensors, as shown in Figure 13 (b) [63]. Theoretically, for a specific tire with a contact pressure of $P(x,y)$ at a location (x,y) inside the contact area with a length of L_0 and width of B_0 , the contact pressure as shown in Figure 13 (a) is [63]:

$$P = \int_{L_0 \times B_0} p(x, y) ds \quad (5)$$

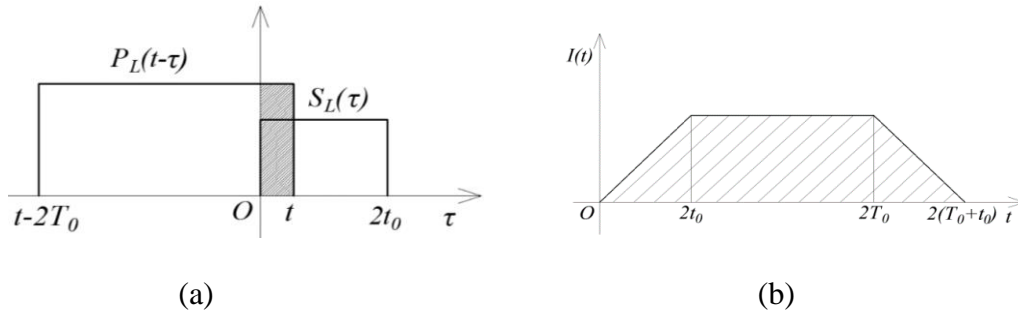


Figure 13. Operation principle to acquire the GFRP-FBG sensor's strain signal by convolution (a) and (b) the expected strain signal

If the embedded GFRP-FBG sensor has a strain sensitivity function, $S_L(t)$, along with the length of the sensor as shown in Fig.4(a), the strain signal, $I(t)$, can be obtained as [63]:

$$I(t) = \int_{-\infty}^{+\infty} P_L(t-\tau)S_L(\tau)vd\tau \quad (6)$$

From Equation 6 and Figure 13, it is clearly demonstrated that a passing vehicle will produce a signal in a trapezoidal shape in the strain response, so does the response of the Bragg wavelength changes of any component of an embedded 3D GFRP-FBG sensor. Since the size of the sensor component is very small between 2.54 cm (1in.) to 5 cm (2 in.) as indicated in Figure 8, and the passing vehicle has a fast driving speed on a regular highway (with speed higher than 45mph), the response to axles of a passing vehicle on the signal of any component of an embedded 3D GFRP-FBG sensor will be more likely in a shape of individual peaks. Figure 14 shows an example of the expected responses of a passing two-axle vehicle for the longitudinal component of the first 3D sensor and the vertical component of the second 3D sensor using the developed sensor network as indicated Figure 12. Figure 14 clearly indicated that each axle of a vehicle would induce a peak in the signal of the FBG sensors. Therefore, the occurrence of an individual peak in

any components of a 3D GFRP-FBG sensor can be used to identify the occurrence of a passing axle and the number of axles of a passing vehicle can then be counted accordingly.

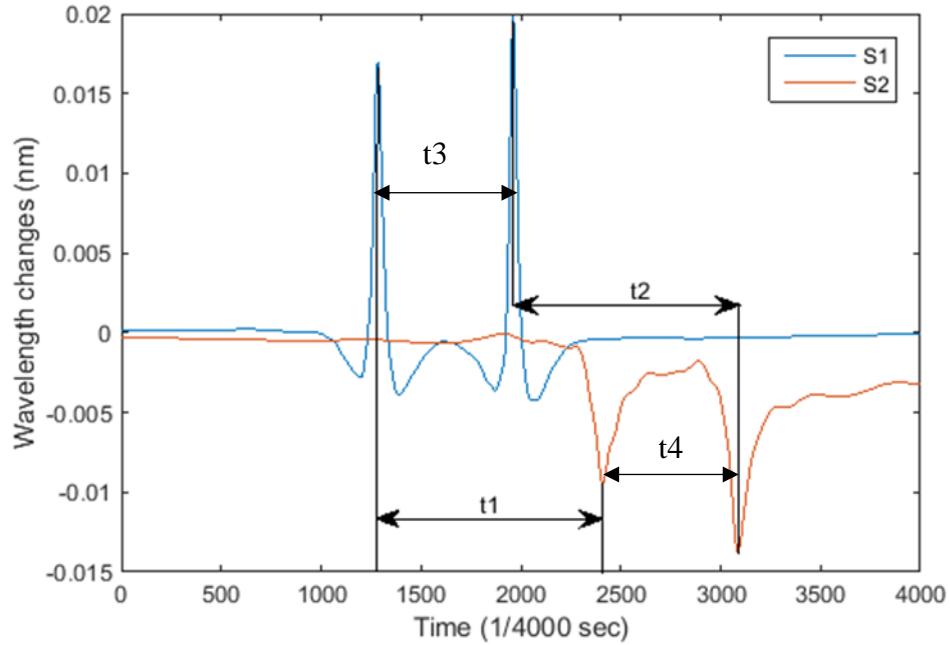


Figure 14. Sensor responses for a passing two-axle vehicle

To derive the wheelbase of a vehicle, it is very important to accurately estimate the vehicle speed. Since the distance between the two sensors in the sensor network, 3D-1 and 3D-2, is a known parameter (D) from the design the sensor network, which was selected to be 4.88 m (16 ft.) in this study, and the time is recorded together with the sensor signal, the vehicle driving speed can then be estimated as:

$$v=D/t. \tag{7}$$

where, D is the distance between the two sensors in the network (4.88 m (16 ft.) in this study), t is the time interval between the peaks of the two sensors for the same axle of a vehicle. Since there are a minimum of two axles for a vehicle, the time intervals can be measured twice by using the first peaks if the two sensors in the network (t_1) and the second peaks of the two sensors (t_2). Thus,

the accuracy of speed estimation can be improved by taking the average of the two adjective sensor peaks as below:

$$v = \frac{\left(\frac{D}{t_1} + \frac{D}{t_2}\right)}{2} \quad (8)$$

Therefore, by knowing the vehicle driving speed, the vehicle's wheelbase can be estimated as:

$$WB = v \cdot t \quad (9)$$

where, t is the time interval detected between two detected peaks of an embedded sensor.

Also, the accuracy of wheelbase estimation can be improved by taking the time estimation average of the two adjective sensor peaks as below:

$$WB = \frac{(v \cdot t_3 + v \cdot t_4)}{2} \quad (10)$$

With the estimation of the number of axles and wheelbase distances, the vehicles can then be classified based on the Federal Highway Administration (FHWA) standard [46].

3.2.2. Vehicle classification using SVM Machine Learning Classifier

According to the FHWA standard [52], vehicles are categorized into the six classes: passenger cars, motorcycles, buses, other 2-axle 4-tire vehicles, single-unit 2-axle 6 tire or more trucks, and combination trucks. In this study, the vehicles are sorted into 3 categories depends on the flow type in the selected case study, as shown in Table 2.

Table 2. Vehicle classes description

Vehicle type	Class	Number of axles	Axles distribution	FHWA category
Small vehicles	C1	2	1F+1R	Passenger car, 2-axle 4-tire vehicle
Medium-large trucks	C2	2	1F+1R	2-axle 4-tire vehicle, 2-axle 6-tire trucks
Single unit trucks-combination of trucks	C3	3-6	1F+2R 1F+2M+2R 1F+2M+3R 1F+1M+1R 1F+1M+2R	single-unit 2-axle 6-tire trucks, or trucks combination

To classify a vehicle into the three categories above, in this paper, the SVM machine learning classifier is applied. The SVM classifies by mapping the data from an input space with an appropriate kernel function into a high dimensional feature space (hypothesis space) where a linear decision rule can be found based on observing the principle of maximizing the margin [64, 65]. Since the vehicle classification is a multi-class problem, as seen in Table 2, two SVM methods can be considered, including the One-Against-All (OAA) and the One-Against-One (OAO) method [66].

The OAA method constructs k SVMs models, where k is the number of classes (vehicle classes). The i th SVM is trained with all of the samples in the i th class with positive labels, and all other samples with negative labels. Thus, given l training data (x_i, y_i) $i=1, \dots, l$, where $x_i \in \mathbb{R}$ and $y_i \in [1, \dots, k]$ which is the class of labels (i.e., vehicle types), the i th SVM solves the following problem:

$$\begin{aligned}
 & \min_{w^i, b^i, \zeta^i} \frac{1}{2} \|w^i\|^2 + C \sum_{j=1}^l \zeta_j^i \\
 & (w^i)^T \phi(x_j) + b^i \geq 1 - \zeta_j^i, y_j = i, \\
 & (w^i)^T \phi(x_j) + b^i \leq 1 - \zeta_j^i, y_j \neq i, \\
 & \zeta_j^i \geq 0, j = 1, \dots, l.
 \end{aligned} \tag{11}$$

where x_i is the training data, where, w is a weight vector, b is a bias, $\phi(x)$ is a nonlinear mapping from the input variable into a high dimensional feature space (Kernel function), $\frac{1}{2} \|w^i\|^2$ controls the complexity of the model, ζ is a slack variable measuring the error on x_i , and C is a regularization parameter.

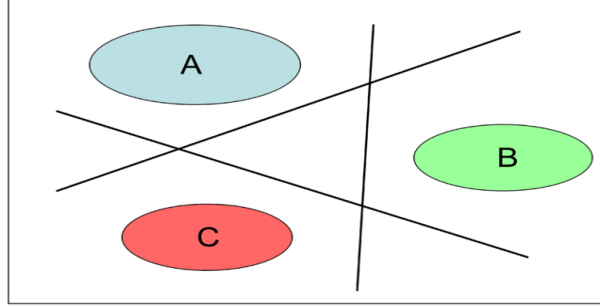


Figure 15. Diagram of binary SVM-OAA region boundaries on a basic problem [67]

The basic goal of SVM machine learning is to find a balance between the complexity term and training error. After solving Equation 11, k decision functions will be generated. Classification of new instances x for the OVA case is done by a winner-takes-all strategy where the classifier with the highest output function assigns the class as shown in Figure 15, the final decision function (d) is:

$$d(x) = \arg \max_{i=1, \dots, k} ((w^i)^T \phi(x) + b^i) \quad (12)$$

On the other hand, the OAO method constructs $k(k-1)/2$ classifiers. For each binary learner, one class is positive, another is negative, and the rest are ignored. This design exhausts all combinations of class pair assignments, as shown in Figure 16. For training data from i th and j th classes, the following binary classification problem is solved:

$$\begin{aligned}
& \min_{w^{ij}, b^{ij}, \zeta_m^{ij}} \frac{1}{2} \|w^{ij}\|^2 + C \sum_{m=1}^l \zeta_m^{ij} \\
& (w^{ij})^T \phi(x_m) + b^{ij} \geq 1 - \zeta_m^{ij}, y_m = i, \\
& (w^{ij})^T \phi(x_m) + b^{ij} \leq 1 - \zeta_m^{ij}, y_m = j, \\
& \zeta_m^{ij} \geq 0, m = 1, \dots, l.
\end{aligned} \tag{13}$$

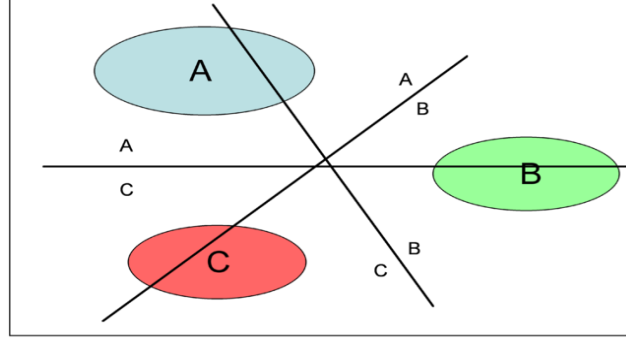


Figure 16. Diagram of SVM-OAO decision boundaries on a basic problem [67]

For the OAO method, classification is done by Max Wins voting strategy, in which every classifier assigns the instance to one of the two classes, then the vote for the assigned class is increased by one vote, and finally the class with the most votes determines the instance classification, the final decision function (d) is:

$$d(x) = \arg \max_j \sum_{i=1}^m |(w^{ij})^T \phi(x_m) + b^{ij}| \tag{14}$$

In order to solve the vehicle classification problem, MATLAB Classification toolbox was used in this paper for multi-class classification problems. Using an SVM method requires dividing the collected data into two datasets, including the training data to train the classification system and the test dataset to validate the trained classification model. From Equations 12 and 14, selecting an appropriate kernel function to map the data from input space to high dimension feature space is the key. There are many types of Kernel functions, including linear, polynomial, sigmoid, and radial basis function (RBF). The RBF was selected in this study due to the facts that the RBF samples into a higher dimensional space so that it can do the nonlinear analysis in addition to fewer

numerical difficulties and less complex than polynomial [68]. The Gaussian RBF used can be expressed as:

$$K(x_i, x_j) = \exp\left(-\frac{\|x_i - x_j\|^2}{2\sigma^2}\right), \sigma > 0 \quad (15)$$

There are two key parameters for an RBF model, including the penalty (C) and Gaussian kernel function parameter (σ) which should be evaluated prior to the model training. Cross-validation through MATLAB classification toolbox includes partitions data into n randomly chosen folds of roughly equal size. One subset is used to validate the model trained using the remaining subsets. This process is repeated n times with different values of C and σ , such that each subset is used exactly once for validation. The values of C and σ which gave the largest cross-validation rate will be used to train the whole train dataset model.

Since the multiple data sources can give a more efficient performance and yield higher accuracy, a centralized fusion strategy was used in this paper, as shown in Figure 17. This strategy collects parameters from data sources and combines them to form one input dataset; then a multi-class SVM is trained to decide on vehicle classes.

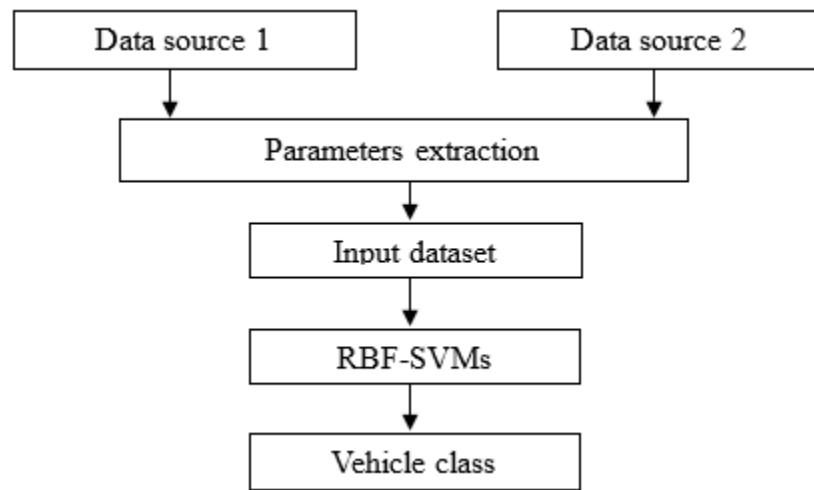


Figure 17. Data fusion strategy scheme

3.3. Field Validation and Discussion

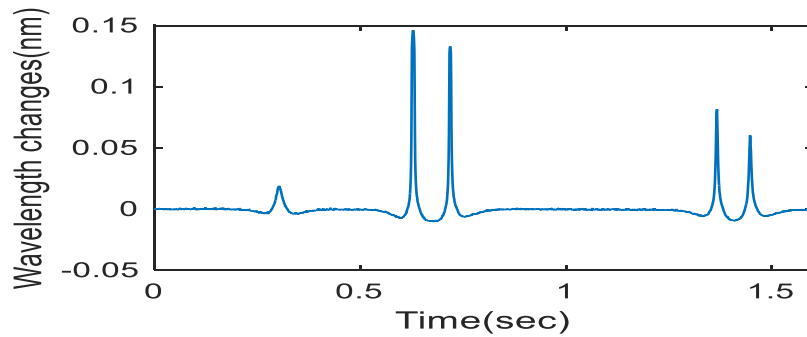
Following Section 3.1, a sensor network of two 3D GFRP-FBG sensors was used for vehicle classification. In addition to the embedded sensor network, a radar gun and a video recording camera were installed on the roadside to obtain the reference for comparison to validate the developed system.

3.3.1. Vehicle parameters identification

Figure 18 (a) shows a five-axle MnROAD semi-truck and Figure 18 (b) shows the S1 sensor response for the MnROAD semi-truck at passing speed of 35 mph. In Figure 18, the sensor clearly identifies each axle of the truck. In addition, the space between peaks is consistent with the wheelbase and the magnitude of each peak is proportionate with the axle weight.



(a)



(b)

Figure 18. MnROAD semi-truck (a), and sensor's response characteristic for five-axle truck (b)

The speed measurement results from the vehicle classification system were compared with the results from a radar gun to validate the system measurement accuracy. The five-axle semi-truck drove on the top of the sensor network at three different speeds, 11.176 m/sec (25mph),

15.646 m/sec (35mph), and 18.776 m/sec (45mph), as shown in Figure 19 for the responses from S1 of Sensor 3D-1 in the network. The truck has estimated actually for the wheelbase distances of 5.194, 1.384, 10.287, and 1.270 meters, respectively. Table 3 shows the comparison of the speeds and wheelbase measurements between the estimated values from the developed system and that from the reference calculated from the radar gun and the recording camera. The measured results from the developed system in Table 3 were obtained using Equations 8 and 10. From Table 3, the system can estimate the speed with an accuracy of 99% or higher and estimate the wheelbase with accuracy higher than 95%.

Table 3. Proposed system measurements for the 5-axle truck

Number	V(ft/sec)	Actual V(ft/sec)	V-error (%)	WB(ft)	Actual WB(ft)	WB-error (%)
1	36.89	36.667	0.61	16.953	17.042	0.52
2	36.89	36.667	0.61	4.744	4.542	4.45
3	36.89	36.667	0.61	33.806	33.75	0.17
4	36.89	36.667	0.61	4.268	4.167	2.42
5	51.912	51.333	1.13	17.048	17.042	0.04
6	51.912	51.333	1.13	4.719	4.542	3.90
7	51.912	51.333	1.13	33.629	33.75	0.36
8	51.912	51.333	1.13	4.192	4.167	0.60
9	62.943	61.6	2.18	17.202	17.042	0.94
10	62.943	61.6	2.18	4.721	4.542	3.94
11	62.943	61.6	2.18	33.609	33.75	0.42
12	62.943	61.6	2.18	4.183	4.167	0.38

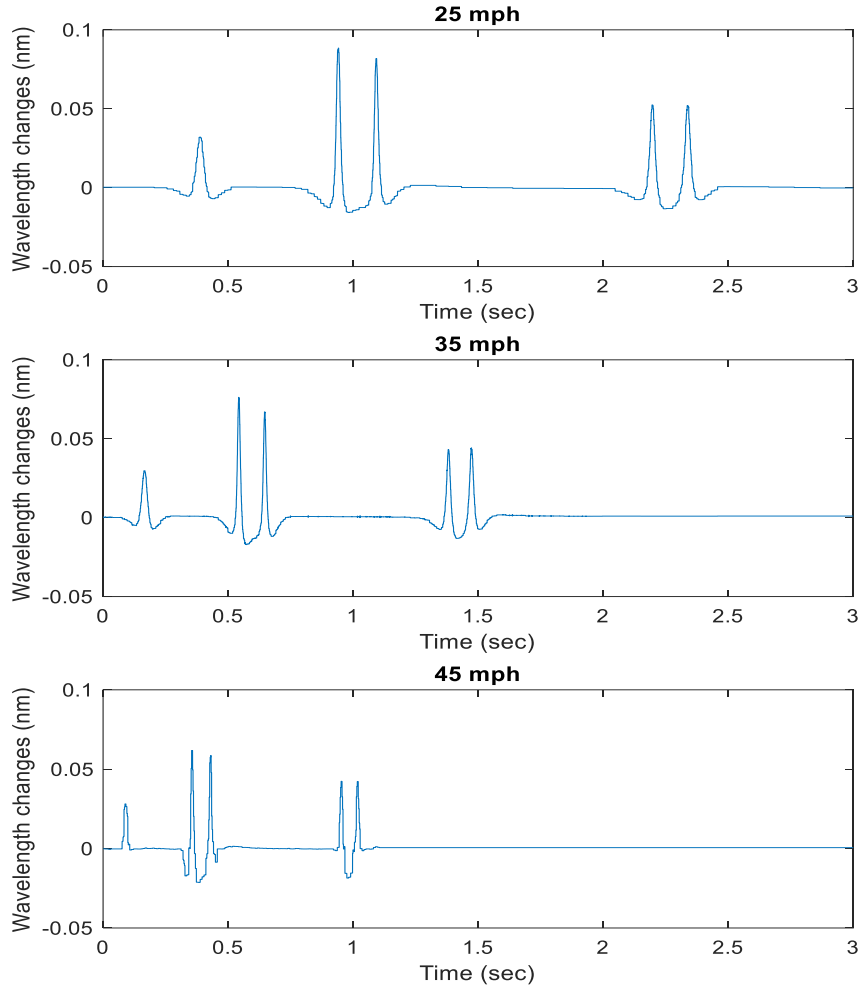


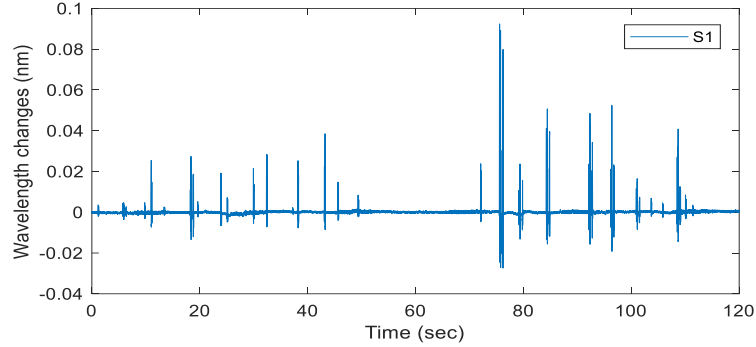
Figure 19. S1 sensor’s responses for five-semi axle truck at 11.176 m/sec (25mph), 15.646 m/sec (35mph), and 18.776 (45mph)

3.3.2. Vehicle classification results

The sensor network on the Cell 17 of Highway I94 in Fig. 8 was then subjected to real traffic for two hours in August 2017, as shown in Figure 20 (a). A total of 477 vehicles were recorded during the acquisition period. Figure 20 (b) shows a figure of an example signal for 2 minutes from the sensor network.



(a)



(b)

Figure 20. Real traffic (a), and S1 sensor's response for 2 minutes of real traffic (b)

The records included a wide variety of vehicle types, ranging from 2-axle passenger cars to 6-axle semi-trailer trucks. A video camera was also used to identify the vehicle type as reference for validating the proposed system. The vehicle parameters (number of axles, N , and wheelbase distances, WB) are extracted from each sensor response. Each sensor in the network has 6 attributes for the two features (N and WB) from sensor response and a class attribute (3 categories, $C1$, $C2$, and $C3$). Therefore, two datasets from S1 and S2 data are constructed:

$$\begin{aligned}
 S1: & (N_1^1, WB_1^1, WB_2^1, WB_3^1, WB_4^1, WB_5^1, Category) \\
 S2: & (N_2^2, WB_1^2, WB_2^2, WB_3^2, WB_4^2, WB_5^2, Category)
 \end{aligned} \tag{16}$$

The recorded dataset for each vehicle type ($C1$, $C2$, and $C3$) are divided into a training set (50% of the data) with 241 vehicles, validation set (25% of the data) with 117 vehicles, and test set (25% of the data) with 117 vehicles of randomly selected records. Table 4 shows the detail numbers of vehicles in each class for all the three-data set. From Table 4, it is clear that most of

the records belong to C1 class because C1 class covers a wider range of vehicle types more than C2 and C3. In total, the training set together with the test set, there are 198 C1 vehicles (133 for training and 65 for test), 32 C2 vehicles (22 for training and 11 for test), and 128 C3 vehicles (86 for training and 42 for test).

Table 4. Collected data

Class	Training set	Validation set	Test set
C1	133	65	65
C2	22	11	11
C3	86	42	42

In this study, two different multiclass SVM classification algorithms (OAA and OAO) were applied. Table 5 shows the estimated vehicle classification from the OAO algorithm. From Table 5, it can be seen that by using OAO algorithm, the system predicts 196 vehicles from the 198 class C1 with 99% accuracy, 31 vehicles from the 33 class C2 with a measurement accuracy of 94%, 128 vehicles from the 128 class C3 with 100% accuracy.

Table 5. OAO estimated vehicle classification

		Predicted class		
		C1	C2	C3
Actual class	C1	196	2	0
	C2	2	31	0
	C3	0	0	128

Table 6 shows the estimated vehicle classification from the OAA algorithm using the proposed strategy. The OAA has the same prediction accuracy for class C1 and C3 vehicles, but for 33 class C2, it predicts 30 class vehicles from the 33 class C2 with an accuracy of 91%.

Table 6. OAA estimated vehicle classification

		Predicted class		
		C1	C2	C3
Actual class	C1	196	2	0
	C2	3	30	0
	C3	0	0	128

Tables 5 and 6 show that both the OAO and OAA algorithms work well for the developed system to classify vehicles with real traffic. The vehicle classification accuracy of the developed system is higher than 90% for both algorithms. The OAO method (>94% accuracy) has slightly higher accuracy than OAA method (>90% accuracy). For class C3 vehicles, since they have significantly different wheelbase distance, both methods predicted 100% correctly for classification. For class C1 and C2, classification error for both algorithms occurred majorly because these two categories share the same number of axles with C2 containing medium trucks (2-axle) which have an average wheelbase distance close to the average of some vehicles in class C1 for the minivan and pick-up trucks (2-axle).

In order to determine the efficiency of using SVM for vehicle classification. The results for the same data input and distribution using SVM are compared with results of using Neural Network (NN) and K Nearest Neighbor (KNN) method.

Neural networks consist of several processing elements called neurons. It is a complicated, non-linear, dynamic system. A two-layer feedforward network has been used in this study. From Table 7, it can be seen that by using NN algorithm, the system predicts 194 vehicles from the 196 class C1 with 99% accuracy, 31 vehicles from the 33 class C2 with a measurement accuracy of 94%, 128 vehicles from the 128 class C3 with 100% accuracy.

Table 7. NN estimated vehicle classification

		Predicted class		
		C1	C2	C3
Actual class	C1	194	2	0
	C2	2	32	0
	C3	0	0	128

A very common non-parametric method is the k-nearest neighbors (kNN) classifier, which is simple but proved effective in many cases. For a data record t to be classified, its k nearest neighbors are computed. Most of the times, majority voting among the data records in the

neighborhood is used to decide the classification for t with or without consideration of distance-based weighting [69]. From Table 8, it can be seen that by using KNN classifier, the system predicts 195 vehicles from the 198 class C1 with 98.5% accuracy, 30 vehicles from the 33 class C2 with a measurement accuracy of 90%, 128 vehicles from the 128 class C3 with 100% accuracy.

Table 8. KNN estimated vehicle classification

		Predicted class		
		C1	C2	C3
Actual class	C1	195	3	0
	C2	3	30	0
	C3	0	0	128

The results from SVM-OAO and KNN have slightly higher accuracy than KNN and SVM-OAA. SVM-OAO and NN based classification system have an average accuracy of 97.5%, followed by SVM-OAA and KNN with an average accuracy of 96 %. The difference between algorithms performance for vehicle classification is not significantly clear, and that may be because of the small data set used in this study.

3.4. Vehicle Counts

Accurate traffic volume estimations on various road segments are critical to the appropriate roadway features geometric design, traffic demand planning, and administrative purposes. State departments of transportation (DOTs) and local transportation agencies traditionally have used traffic volume count programs to evaluate the need for appropriate traffic control and geometric improvements.

Vehicle counting can be defined as the activity of measuring and recording traffic characteristics such as vehicle volume, classification, speed, weight, or a combination of these characteristics [12]. Typically, there are two methods for counting traffic: manual and automatic counting.

The proposed sensor network has been used for validation. Figure 21 shows the sensor's responses on its vertical and longitudinal components for a range of vehicle categories, including passenger car, two-axle vehicle, three-axle vehicle, and five-axle vehicle. The average speed range for the identified vehicles was between 65 mph and 75 mph. It is obvious that the vertical and longitudinal components responses show the ability of the sensor to detect each axle of the traveled vehicle with different responses proportionate to the tire weight. Also, over 3 months of testing, the sensors functioning on the I-94 freeway did not appear to have any deterioration in performance. Figure 22 shows the sensor's response on its longitudinal component for a 250 second monitoring period. During this period 23 vehicles passed over the sensor, with a total of 69 axles. The counting of axles and vehicles was done by tracking the peaks through the sensor's response.

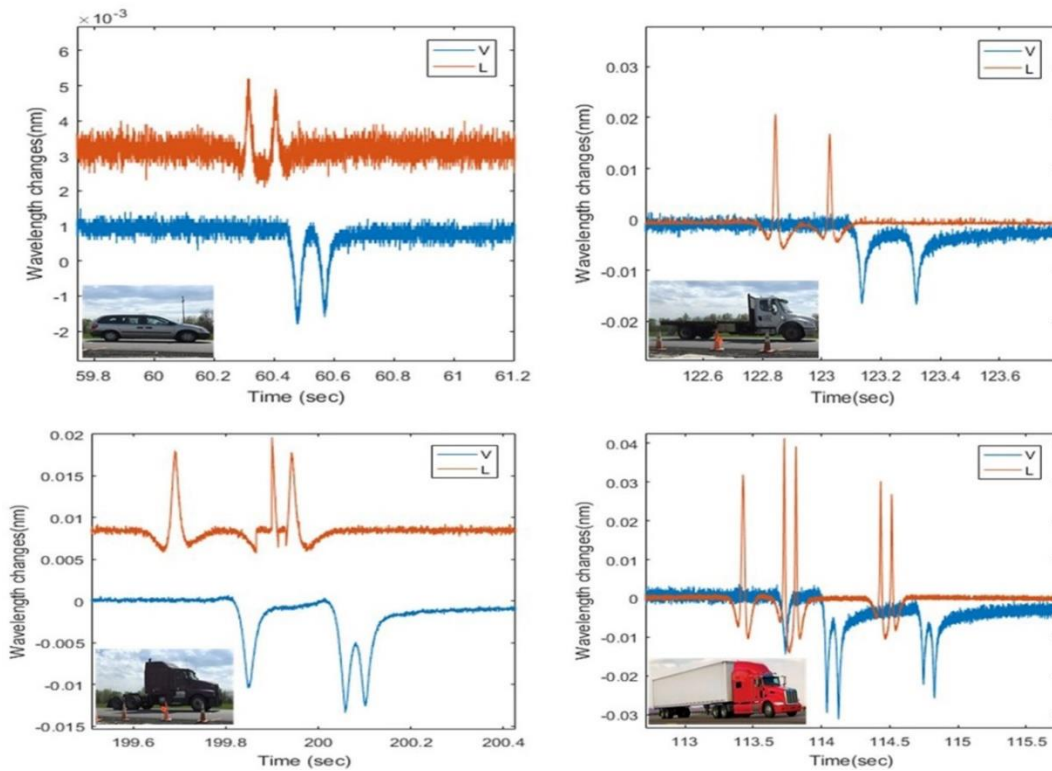


Figure 21. Sensor response for different vehicle class

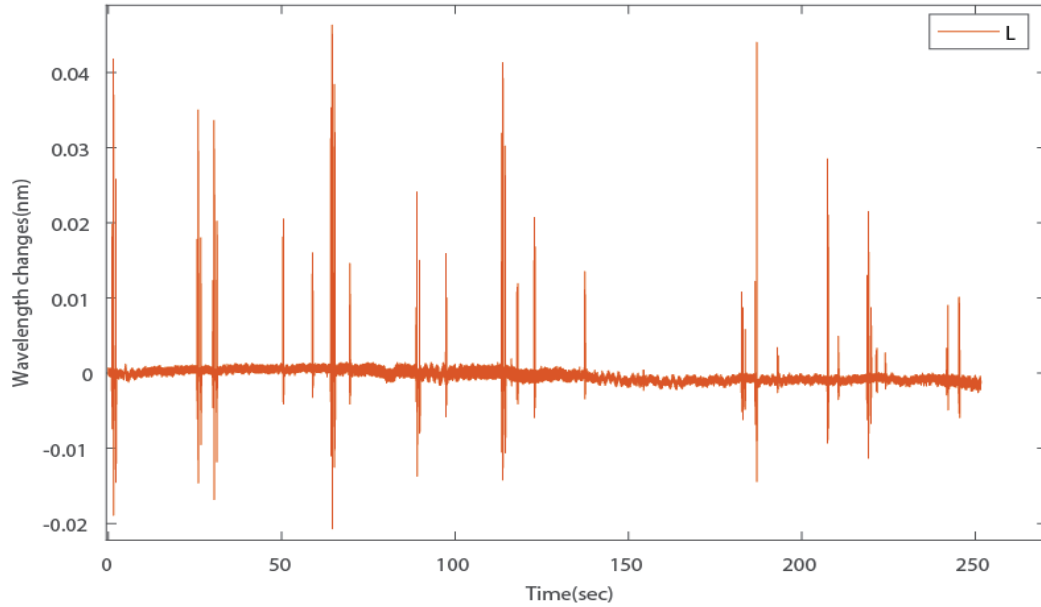


Figure 22. Sensor response for 250 seconds period

3.5. Summary

In this Chapter, a vehicle classification system based on glass fiber-reinforced polymer packaged fiber Bragg grating sensors (3D GFRP-FBG) network. The vehicle's speed and wheelbase can then be estimated according to the different time a vehicle arrived at the sensor sites, and speeds monitored from the wavelength changes of the in-pavement sensors. The vehicle classification system uses support vector machine (SVM), Neural Network (NN), and K-Nearest Neighbor (KNN) learning algorithms to classify vehicles into categories ranging from small vehicles to combination trucks. The field-testing results from real traffic show that the results from SVM-OAO and KNN have slightly higher accuracy than KNN and SVM-OAA. SVM-OAO and NN based classification system have an average accuracy of 97.5%, followed by SVM-OAA and KNN with an average accuracy of 96 %. The difference between algorithms performance for vehicle classification is not significantly clear, and that may be because of the small data set used in this study. Also, the system shows that ability to perform counting of axles and vehicles by tracking the peaks through the sensor's response.

4. WIM MEASUREMENTS IN FLEXIBLE PAVEMENT

Estimation the vehicle's weight is a controlling factor in flexible pavement design, also with significant weight's effect on the road maintenance costs and the safety of road users. The flexible pavement experiences dynamic load rather than static weight which is still used in pavement design guide, such as equivalent single axle loads (ESAL) which is used by the American Association of State Highway and Transportation Officials (AASHTO) pavement design guide to represent the vehicle loads in pavement design [70]. Currently, there are new methods that use axle load spectra to represent the vehicle loads in pavement design, such as the Mechanistic-Empirical Pavement Design Guide (MEPDG) [71]. Hence, the dynamic load from the vehicles have become important to be estimated.

4.1. 3D GFRP-FBG Sensor for WIM Measurements

When a vehicle passes over the road, the pavement produces strain signals which will be picked up by wavelength changes of the embedded 3D GFRP-FBG sensor as shown in Equation 4. The strain signal inside the pavement is formed from the convolution of the load from the tire contact area and the sensitivity function of the embedded 3D GFRP-FBG sensor, as explained in Section 3.2.1.

Currently, there are three theories to analyze flexible pavement, the simplest way to characterize the behavior of the flexible pavement is to consider it as homogenous half-space with infinite surface area and depth of the pavement. The original theory by Boussinesq can be used to determine the stress, strain, and deflections in the subgrade if the modulus ratio between the pavement and subgrade is close to unity but Flexible pavements are layered systems with better materials on top and cannot be represented by a homogeneous mass [72].

Since the Hot Mix Asphalt (HMA) is regarded as viscoelastic material whose behavior depends on the time of loading, so it is natural to apply the theory of viscoelasticity to analyze the flexible pavement. There are two general methods for characterizing viscoelastic materials: one by a mechanical model, the other by a creep-compliance curve [72].

The flexible pavements are a layered system, so the use of Burmister's layered theory is more appropriate. The basic assumptions of this theory are as follows [72]:

- 1) Each layer is homogeneous, isotropic, and linearly elastic;
- 2) The material is weightless and infinite in areal extent;
- 3) Each layer has a finite thickness h , except that the lowest layer is infinite in thickness;
- 4) A uniform pressure q is applied on the surface over a circular area of radius a .

In this study, the multilayer system theory is used to determine stress and strain through the flexible pavement, because it is appropriate to characterize the behavior of the flexible pavement rather than homogenous mass and simplicity regards to viscoelastic solutions.

In this study, the 3D GFRP-FBG sensor is assumed to be embedded inside a flexible pavement with i layers. The circular contact pressure area of radius a . Each layer has three parameters: modulus of elasticity E , Poisson's ratio ν and depth have shown in Figure 23. By applying the classical theory of elasticity and considering that x -direction is the longitudinal direction of the 3D GFRP-FBG sensor which is parallel to the wheel path, y -direction is the transverse direction of the sensor which is perpendicular to the wheel path, and z -direction is the vertical direction of the sensor which is beneath the asphalt surface. The strain components under the circularly loaded area in the three directions can be found as follow [72]:

$$\varepsilon_V = \frac{P}{E\pi a} \alpha \int_0^{\infty} -m J_0(m\rho) [A_i - C_i(1 - 2\nu_i - m\lambda)] e^{-m(\lambda_i - \lambda)} + [B_i + D_i(1 - 2\nu_i - m\lambda)] e^{-m(\lambda - \lambda_i - 1)} \frac{J_1(m\alpha) dm}{m} \quad (17)$$

$$\varepsilon_L = \frac{P}{E\pi a^2} \alpha \int_0^\infty \left([mJ_0(m\rho) - \frac{J_1(m\rho)}{\rho}] [A_i - C_i(1+m\lambda)] e^{-m(\lambda_i-\lambda)} + [B_i + D_i(1-m\lambda)] e^{-m(\lambda-\lambda_i-1)} + 2v_i m J_0(m\rho) [C_i e^{-m(\lambda_i-\lambda)} - D_i e^{-m(\lambda-\lambda_i-1)}] \right) \frac{J_1(m\alpha) dm}{m} \quad (18)$$

$$\varepsilon_T = \frac{P}{E\pi a^2} \alpha \int_0^\infty \left(-\frac{J_1(m\rho)}{\rho} [A_i - C_i(1+m\lambda)] e^{-m(\lambda_i-\lambda)} + [B_i + D_i(1-m\lambda)] e^{-m(\lambda-\lambda_i-1)} + 2v_i m J_0(m\rho) [C_i e^{-m(\lambda_i-\lambda)} - D_i e^{-m(\lambda-\lambda_i-1)}] \right) \frac{J_1(m\alpha) dm}{m} \quad (19)$$

where ε_V is vertical strain, ε_L is the longitudinal strain (parallel to the wheel path), ε_T is the transverse strain (perpendicular to the wheel path), r and z are the cylindrical coordinates for radial and vertical directions, P is the load, α is a/h , A , B , C , and D are constant of integration, ρ is r/h , λ is z/h , m is a parameter, and J_0 and J_1 are Bessel functions.



Figure 23. Flexible pavement cross-section

As mentioned above, the multi-layer system is used to determine stress and strain in the flexible pavement. Since it is hard to analyze flexible pavement theoretically; the KENLAYER software is used in this study to determine the strains at the sensor location and to perform sensitivity study. The KENLAYER computer program is established by Huang [72] applies only to flexible pavements. The fundamental of KENLAYER is the solution for an elastic multilayer system under a circularly loaded area. KENLAYER can be applied to determine stress, strain, and

deflection at any point in the layered systems under single, dual, dual-tandem, or dual-tridem wheels with each layer behaving differently. The theoretical development of KENLAYER software is discussed in detail by Huang [72].

Thus, the strain transfer function can be obtained by combining Equations 4, Strain results from KENLAYER, and the strain transfer rate of the GFRP to host material, ϕ [45], which is related to the modulus of the elasticity of the host material, E . The transfer function of the GFRP-FBG sensor for WIM measurement in three directions (longitudinal, transverse, and vertical direction), therefore, can be represented as below:

$$P = A_L \left(\frac{\Delta\lambda_L}{\lambda_L} - \frac{\Delta\lambda_{Te}}{\lambda_{Te}} \right) = A_T \left(\frac{\Delta\lambda_{Tr}}{\lambda_{Tr}} - \frac{\Delta\lambda_{Te}}{\lambda_{Te}} \right) = A_V \left(\frac{\Delta\lambda_V}{\lambda_V} - \frac{\Delta\lambda_{Te}}{\lambda_{Te}} \right) \quad (20)$$

in which, λ_L , λ_{Tr} , λ_V , and λ_{Te} are the measured center wavelengths from longitudinal, transverse, vertical components of the 3D GFRP-FBG sensor and the temperature compensation sensor, respectively. The A_L , A_T , and A_V are the weight sensitivity of the GFRP-FBG sensor for WIM measurements in longitudinal, transverse, and vertical directions, respectively. In order to get the weight sensitivity functions of the GFRP-FBG sensor for the three components, the strain at the locations of the three components are calculated for one-unit load using KENLAYER software and represented as ε_L , ε_T , and ε_V for longitudinal, transverse, and vertical component respectively. Thus, the weight sensitivity of the GFRP-FBG sensor for WIM measurements for the three components can be represented as follows:

$$A_L = \frac{1}{\varepsilon_L \phi (1 - P_e)}; A_T = \frac{1}{\varepsilon_T \phi (1 - P_e)}; A_V = \frac{1}{\varepsilon_V \phi (1 - P_e)} \quad (21)$$

4.2. Sensitivity Study

From Equations 21, it is clearly seen that the sensitivity of the 3D GFRP-FBG sensor for WIM measurement in all three dimensions will be significantly influenced by different factors such as sensor installation depth (z), host material property (E), and the location of the wheel path

(I). In this section, the influences of all these parameters on the 3D GFRP-FBG sensor for the WIM measurements will be investigated.

4.2.1. Sensor depth (z)

Numerical simulations on the sensitivity of the installation depth on the sensor's performance is performed using KENLAYER software and Equations (20 and 21) by changing the installation depth, z , and fixing all the other parameters. Figure 24 shows the changes of the 3D GFRP FBG sensor's WIM measurement sensitivity with various installation depths in longitudinal, transverse, and vertical directions, respectively. Figure 24 shows that the installation depth significantly influences the sensor's behavior for WIM measurement. The simulation assumes the elastic modulus of the asphalt concrete to be 3447.4 Mpa (500 ksi), and the wheel path to be directly loaded right above the vertical component of the 3D sensor on the asphalt surface.

The longitudinal and transverse components of the 3D sensor show highest measurement sensitivity either on the surface of the pavement or on the bottom of the asphalt layer, and the vertical component has the highest sensitivity near to the middle of the HMA layer. If installed on the surface of the pavement, the sensor will be vulnerable to damage, resulting in shorter service life. Thus, the recommended practice is to install the sensor at the bottom of the asphalt concrete layer to secure the best measurement sensitivity. Figure 24 shows that when installing the sensor at the bottom of the asphalt layer, all three components of the 3D sensor are very sensitive to WIM measurements. The vertical component of the 3D sensor is in compression wherever the installation depth is, and it has the largest WIM measurement sensitivity of about -41nm/kips, but still has WIM measurement sensitivity of about -28nm/kips at the bottom of the asphalt layer. The longitudinal and transverse components will be in tension if their position is on the bottom of the

HMA layer with measurement sensitivity around 18nm/kips, which is about 65% of the vertical component at the bottom of the asphalt layer.

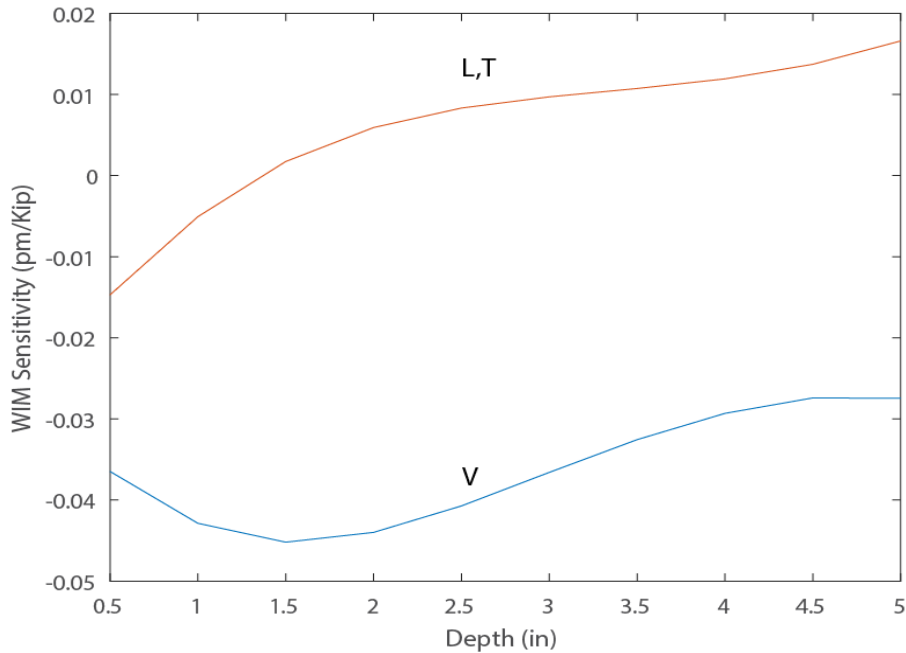


Figure 24. Sensor’s WIM measurement sensitivity changes with sensor depth in longitudinal (L), transverse (T) and vertical (V) directions

4.2.2. Host material property (E)

The authors observed that the material property of the host matrix is very important to any embedded sensors [45] and affects the sensor stability and reliability in service. The modulus of elasticity is the major parameter, which represents the material property of the host matrix. Figure 25 shows the WIM measurement sensitivity changes of the 3D GFRP-FBG sensor for its longitudinal, transverse, and vertical components with a different modulus of elasticity, E, of the asphalt materials. The simulation assumes that the sensor is installed at the bottom of the asphalt layer, and the wheel load is directly applied directly above the vertical component of the 3D sensor on the asphalt concrete surface.

As shown in Figure 25, a softer host matrix (HMA materials) yields higher WIM measurement sensitivity, and the sensor's sensitivity would decrease with an increase in the modulus of the host materials. At a temperature of 70°F, the asphalt has a typical elastic modulus of about 2068.4 Mpa (300 ksi), resulting in measurement sensitivity of -40nm/kips for the vertical component and 18nm/kips for longitudinal and transverse components of the 3D sensor. The changes in the property of the host matrix would affect the performance of the vertical component much more than the other two directions. The sensitivity of the vertical components will dramatically drop from -60 nm/kips to -26 nm/kips, almost 60%, if the modulus of the host matrix varies from 1206.6 Mpa (175 ksi) to 2757.9 Mpa (400 ksi) respectively. However, the longitudinal and transverse components of the sensor show less dependence on the modulus of the host materials with less than a 20% drop when the modulus of the host matrix varies from 1206.6 Mpa (175 ksi) to 2757.9 Mpa (400 ksi). Because asphalt is a viscoelastic material, its elastic modulus changes significantly with temperature and loading rate. The elastic modulus of asphalt will change dramatically between different seasons and even during the course of a single day. For an accurate WIM measurement in practical applications, the authors recommend that the developed 3D GFRP-FBG sensor be further studied for temperature compensations considering the material property changes with temperature and wheel loading rate.

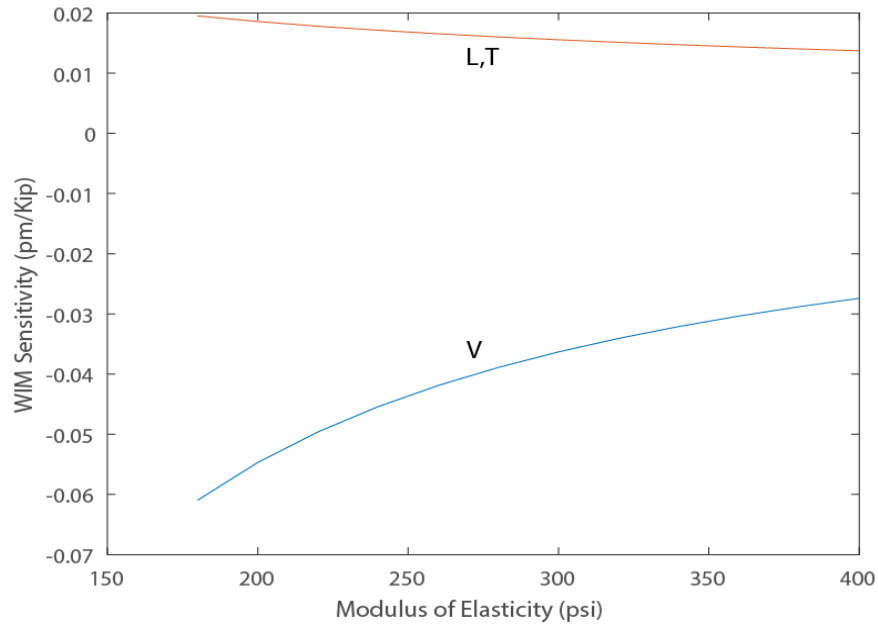


Figure 25. Sensor's WIM measurement sensitivity changes with pavement modulus of elasticity, E, in longitudinal (L), transverse (T) and vertical (V) directions

4.2.3. Load location (l)

Because the developed sensor is a localized sensor, the actual wheel paths of the vehicles, which determine the loading locations on the sensor, are very important for measurement accuracy, stability, and repeatability. Assuming sensors are installed at the bottom of the asphalt concrete layer with an elastic modulus of 3447.4 Mpa (500 ksi), Figure 26 shows the WIM measurement sensitivity changes of the 3D GFRP-FBG sensor's longitudinal, transverse, and vertical components with various physical longitudinal locations of the wheel load.

Figure 26 shows that all sensors' components have maximum WIM sensitivity when the load is applied directly over the sensor. The vertical component is very sensitive to loading locations. In the simulated case, the vertical component will respond to a wheel load longitudinally within 20 cm (8 in.) of the sensor head. The transverse component will respond to a wheel load longitudinally within 30 cm (12 in.) away from the sensor head. Thus, because some trucks may have double or triple tires, which may be within 30 cm (12 in.) space, the WIM measurement for

trucks with multiple tires is a combined effect from the grouped tires. More investigations on the influences of neighboring tires are necessary for an accurate WIM in practice. The longitudinal component will respond in tension when the wheel load is within the depth of the asphalt layer (12.5 cm or 5 in.) and in compression after the wheel load passes the depth of the asphalt layer until it is more than 60 cm (24 in. or 2 ft.) away from the sensor. The axle distance of a vehicle is much bigger than 60 cm (2 ft.), and that leads to little influence from various axles on the sensor's response. Also, in real traffic, especially, in highway traffic, the following distance between vehicles will be significantly larger than 60 cm (2 ft.). Therefore, the influence from nearby vehicles to the sensor will be negligible.

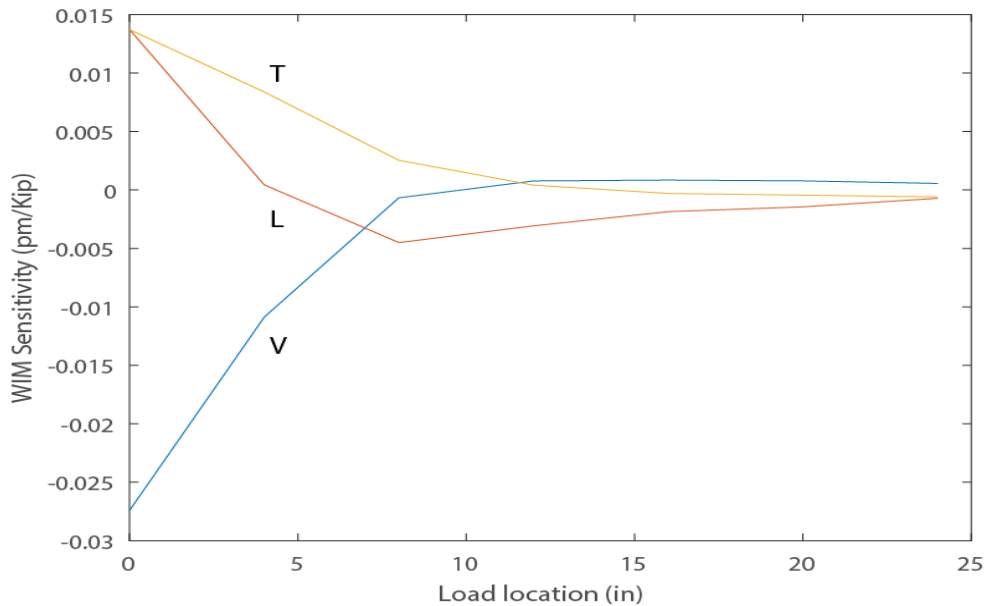


Figure 26. Sensor's WIM measurement sensitivity changes with longitudinal location of the wheel in longitudinal (L), transverse (T) and vertical (V) directions

From Figure 25, 25, and 26, it can be seen that although the vertical component of the 3D sensor has the largest sensitivity, it also depends significantly on the material property changes induced from temperature, loading rates, and loading locations. The vertical component can only respond to a wheel load within 20 cm (8in.) of the sensor head, but in practice, it is very challenging

to ensure the vehicle will pass directly over the sensor head (within a 20 cm (8in.) radius) when driving. The transverse component of the 3D is less dependent on the material property of the host matrix. However, it also requires the wheel load to be within a 30 cm (12in.) radius of the sensor.

On the other hand, the longitudinal component of the 3D sensor has a competitive sensitivity, less dependence on property changes of the host matrix from temperature or loading rate and is sensitive to loads within a 60 cm (24in.) radius. Thus, the longitudinal component of the 3D sensor, which aligns with the traffic wheel path, will be most suitable for WIM measurements and warrants further investigation for practical applications. Based on this field assessment, the authors selected the longitudinal component of the 3D sensor to test the feasibility of the sensor for high-speed WIM measurement.

4.3. Field Validation of a Case Study

4.3.1. Field testing setup

Following Section 3.1, a sensor network of sensor 3D-2 was used for WIM measurements validation. All the sensor components show high sensitivity for WIM measurements, as shown above in sensitivity study. However, vertical and transverse components have worst field results due to the fact that the contact area over the transverse component is much less than longitudinal component and the vertical component was installed in a base layer which yields to a higher error in a strain transfer rate of the GFRP to host material. Thus, the longitudinal component of the 3D-2 sensor was used for WIM measurements validation.

The 3D-2 sensor was installed inside the Pavement, Cell 17. Figure 27 shows the flexible pavement cross section of Cell 17. The cross-section consists of 5 in. of HMA as a wearing layer, 12 in. of gravel base layer, 19 in. of selected material as a sub-base layer, and clay subgrade.

5 in. HMA
12 in. Base layer
19 in. Subbase layer
Subgrade

Figure 27. Cell 17 flexible pavement cross section

In order to construct a KENLAYER model for the above cross-section, all the material properties should be provided, since the HMA material is a visco-elastic material, which means that the modulus of elasticity of the material changes with the load frequency on the material (which can be related to the rolling vehicle speed) and the material temperature. For that purpose, two HMA samples from Cell 17 have been tested to get the dynamic modulus properties of the HMA material following AASHTO standard [73]. The master curve from the dynamic modulus test results has been constructed, as shown in Figure 28. The master curve can relate the modulus of elasticity (E^*) with the reduced frequency (f_r) as shown in Equation 22, where f_r is a function of the shift factor ($a(T)$) as seen in Equation 23. The shift factor is a function of pavement temperature (T) and loading frequency (f) [74].

$$\log|E^*| = \log|E_{\min}| + \frac{\log|E_{\max}| - \log|E_{\min}|}{1 + e^{\beta + \mu \times \log f_r}} \quad (22)$$

$$f_r = f \times 10^{\log(a(T))} \quad (23)$$

where E_{\min} , E_{\max} , β , μ are curve fitting coefficients obtained from the master curve.

The loading frequency is a function of the vehicle speed (v). In the case we assume that there will be no effect when the load is six times contact radius (a) far away from the sensor

location, the travel time on the top of the sensor (T) then is equal to $12a/v$, the loading frequency (f) can be related to the vehicle speed (v) as below:

$$f = \frac{1}{T} = \frac{v}{12a} \quad (24)$$

Thus, the modulus of the flexible pavement can be derived with specific driving speed and temperature.

Table 9 shows the material properties for the Cell 17 pavement cross section. After the installation of the sensor, the 3D-2 longitudinal component was connected to an FBG integrator together with a temperature compensation FBG sensor. The FBG integrator was further connected to a personal computer to record the data. For WIM measurement at low speed, it is not required to have a high sampling frequency of the instrument. Therefore, the sampling rate of the FBG integrator was set to be 100 Hz, but for high speed, the sampling rate was set to be > 1200 Hz to eliminate the dynamic effect as stated by Zhiming et al. [63].

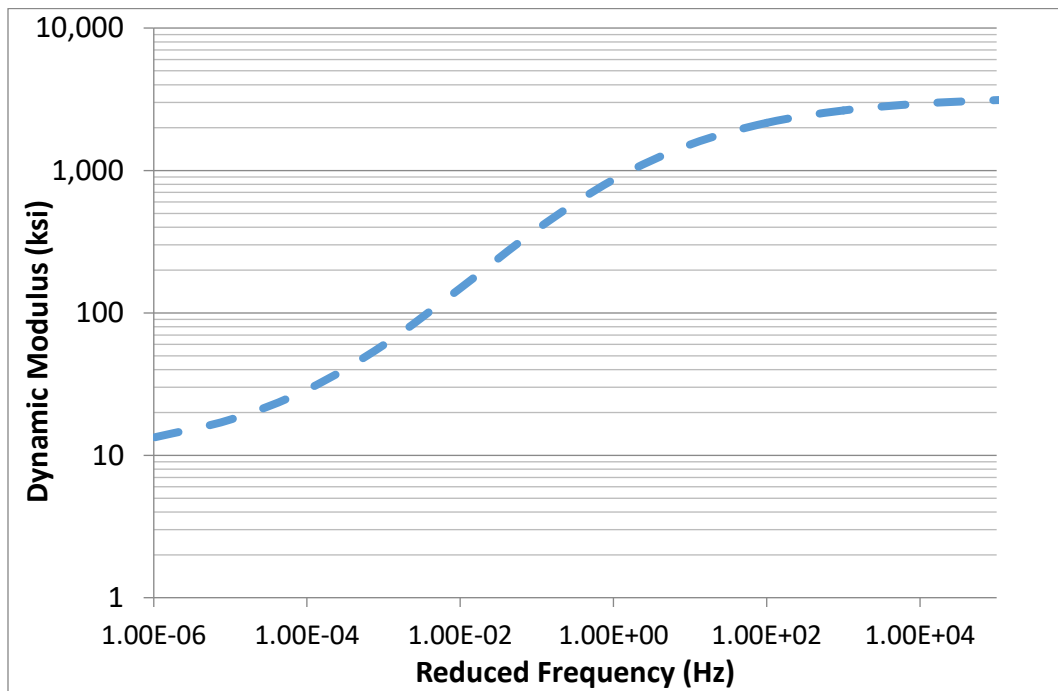


Figure 28. Master curve of Cell 17 HMA dynamic modulus test results

Table 9. Material properties

Layer	Modulus of elasticity(E), Ksi	Poisson's ratio
HMA at 25.2 °C and 5 mph speed	749.9	0.3
HMA at 25.2 °C and 45 mph speed	1349	0.3
Base	60	0.35
Sub-base	40	0.35
Subgrade	12	0.4

4.3.2. Field testing results

To perform the validation tests, a -5-axle semi-truck with a total gross weight of 80 Kips (36.29 tons) was used to generate the weight to be measured in motion. The truck moves on top of the sensor back and forth at 5 mph and 45 mph to validate the sensor for low-speed and high-speed WIM measurements. Figure 29 (a) shows of the axle load distribution of the truck at each axle, and Figure 29 (b) shows the truck dimensions.

In this study, the right wheels of the truck are the weights to be measured which have the flowing weight distribution of 2.63 tons (5.8 kips), 4.11 tons (9.05 kips) , 3.65 tons (8.05 kips), 3.9 tons (8.6 kips), and 3.72 tons (8.2 kips) for first, second, third, fourth, and fifth right wheel, respectively. Since the sensor only measures the weight of a single wheel and estimate the vehicle weight based on the assumption that the weight is equally distributed on each wheel. To reduce the measurement error from this assumption, more numbers of sensors (four sensors or more in parallel) are recommended to be placed as a measurement system for more accurate axle weight measurement in practice if budget allows. Since the sensitivity study shows the significant effect of the load location on the WIM measurements, the truck's driver has been asked to take the road center line as a reference for the left side of the truck, using the truck dimension and with the known distance of the center line from the sensor location, the tire location can be predicted. The longitudinal component of the 3D-2 sensor clearly identifies each axle of the truck.

Figures 30 shows the sensor's responses on its longitudinal components for one truck passed on the Cell 17 pavement at the MnROAD facility in September 2017 at 5 mph and 45 mph vehicle speed.

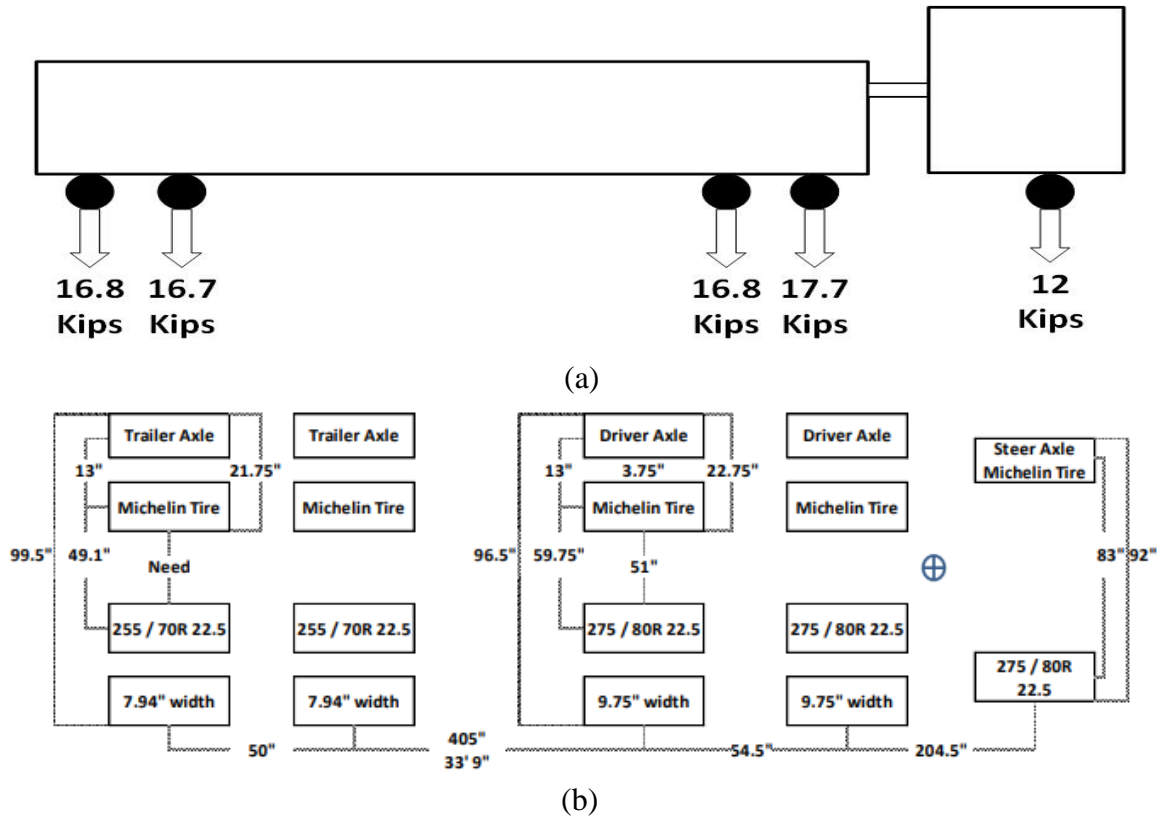


Figure 29. The layout of MnROAD loading truck (a) and the truck dimension (b). (1'=1 ft., 1"=1 in.)

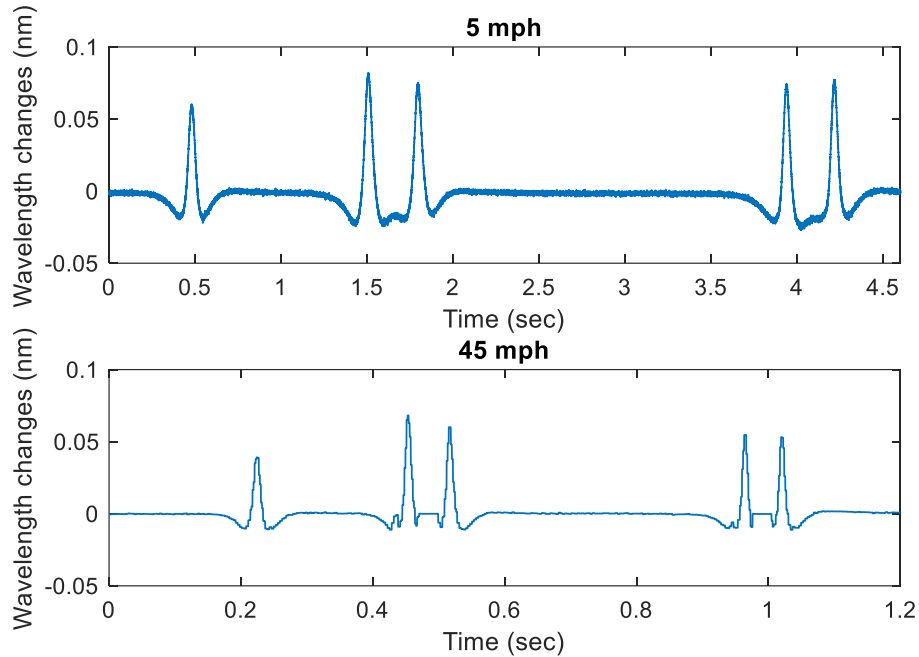


Figure 30. 3D-2 longitudinal sensor’s response at 5 mph and 45 mph vehicle speed

Equations (20 and 21) and the output from the KENLAYER estimated the theoretic WIM measurement sensitivity (S) for each axle of the longitudinal component of the 3D sensor as shown in Table 10 (unit: 10^{-6} nm/kip). From Table 10, the average theoretic WIM measurement sensitivity of the longitudinal component of the 3D sensor is 5.19×10^{-6} nm/kip and 6.98×10^{-6} nm/kip at 45 mph and 5 mph, respectively. According to the calculated sensitivity and the measured wavelengths in Figure 30, Table 11 summarizes the WIM measurements from the longitudinal component of the 3D-2 sensor for each truck axle at 5 mph and 45 mph.

Table 10. Estimated theoretic sensitivity (s) [unit: 10^{-6} nm/Kip]

Speed	S1	S2	S3	S4	S5	Avg S
5 mph	8.25	6.51	6.55	6.86	6.71	6.98
45 mph	5.47	4.99	5.00	5.31	5.16	5.19

Table 11. Field WIM measurements from the sensor at 5 mph and 45 mph

Speed		Axle 1	Axle 2	Axle 3	Axle 4	Axle 5
5 mph	<u>Wavelength changes (pm)</u>	60	82	74	74	77
	<u>WIM (kips)</u>	4.5	8.15	7.31	6.98	7.4
45 mph	<u>Wavelength changes (pm)</u>	42	71	65	58	57
	<u>WIM (kips)</u>	4.37	8.82	8.28	6.94	7.27

4.3.3. Field test results discussion

Table 12 compares the WIM measurements from the longitudinal of the 3D-2 sensor with the reference weights for each truck axle at 5 mph and 45 mph vehicle speed. When compared with the reference weight which are the actual weights of the truck tires, the longitudinal component of the sensor has a measurement accuracy of 86.3% and 89.5% at 5 mph and 45 mph vehicle speed, respectively. This study serves as a preliminary study to investigate the feasibility of the GFRP-FBG sensor for WIM system in flexible pavement. It can be seen from Table 12 that there is a big variance of measurement error between different axles, which may majorly be contributed by the variance of loading position for each axle. Due to the fact that the 3D sensor is still categorized as a point sensor and the loading position for each axle is not exactly the same when the vehicle is passing the sensor location, this error may be significant. In the future, the actual influence of loading positions of each axle on the sensor measurement error should be further studied and will be reported later. In addition, there are some other error sources such as temperature estimation, driving speed, and dynamic modulus estimation. These contributing factors on measurement accuracy will also need to be investigated in a future study.

Table 12. Comparison of the WIM measurements with references

Measured Weight	Axle 1		Axle 2		Axle 3		Axle 4		Axle 5	
	WIM (Kips)	Error (%)								
Reference	5.8	-	9.05	-	8.05	-	8.6	-	8.2	-
5 mph	4.5	21.9	8.15	9.9	7.31	9.14	6.98	18.82	7.4	9.34
45 mph	4.37	14.32	8.82	1.9	8.28	4.49	6.94	17.8	7.27	12.7

4.4. Summary

In this Chapter, the proposed sensor network has been validated for low-speed and high-speed WIM measurements in flexible pavement. The transfer function has been derived using strain-wavelength relation and strain results from KENLAYER software, the performed sensitivity study shows that the GFRP-FBG sensor is very sensitive to the sensor installation depth and the best performance for WIM measurements is to install the sensor at the bottom of the pavement sections. Also, the sensor's WIM measurement sensitivity will decrease with the increase of the modulus of the embedded host materials. If the modulus increases twice, the sensitivity of the sensor for all the three components will decrease almost half for the WIM measurement. All sensor's components have maximum WIM sensitivity when the load is applied directly over the sensor. Also, the WIM sensitivity of all sensor's components tends to zero after one foot. Field testing validated that the longitudinal component of the sensor has a measurement accuracy of 86.3% and 89.5% at 5 mph and 45 mph vehicle speed, respectively.

5. PARAMETRIC STUDY

At the first stage of the development of the WIM system, the variation in the wheel load of a moving vehicle was the only parameter significantly contributes to the inaccuracy of weighing measurements. However, an analytical study stated that there were additional factors significantly affect the weight measurement of a moving vehicle [75], including, the temperature of the pavement, road roughness, vehicle speed, vehicle's suspension system, weather conditions, etc. These factors affect the weight measurements, regardless of the sensor technology. Basically, these factors can be divided into two categories according to the source of their occurrence (WIM system or vehicle), or the degree of influence on the weight measurements (major or minor) as shown in Figure 31.

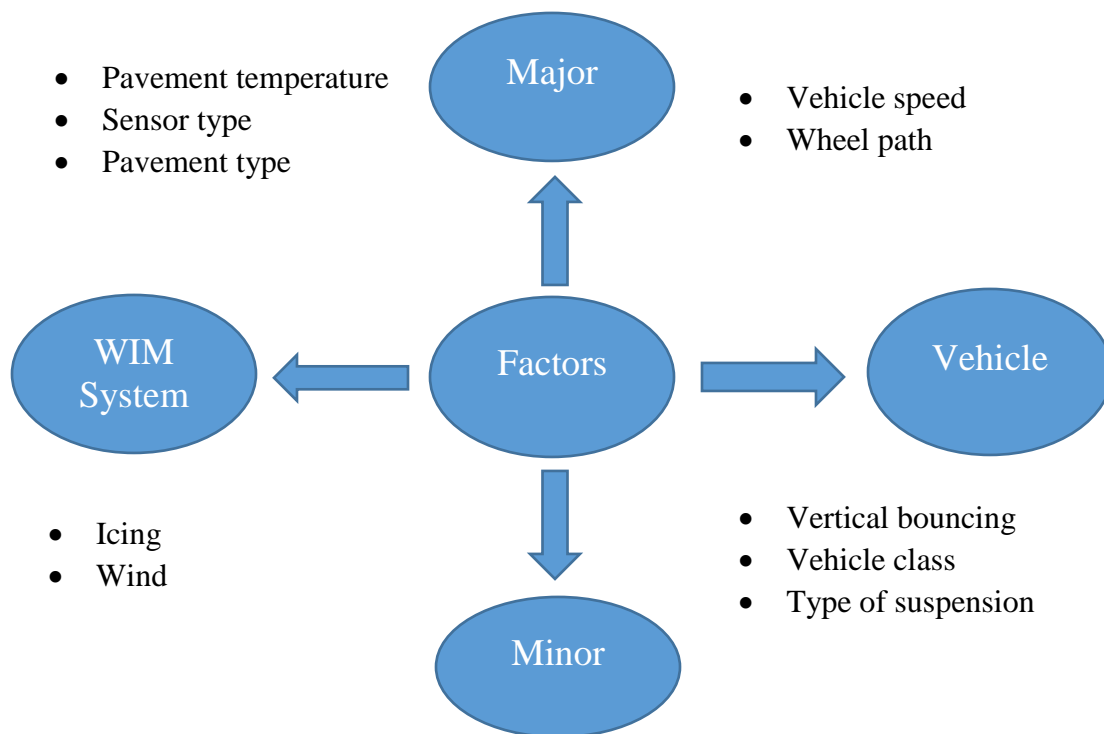


Figure 31. Factors affecting the WIM system measurements accuracy

From Figure 31 and the performed feasibility study in Chapter 4, it can be seen that to apply the new developed 3D-GFRP-FBG sensors for traffic monitoring; it is urgently needed to have an insightful study of the significant factors and their effect on the weight measurements. Since this study focuses on the newly developed 3D-GFRP-FBG in flexible pavements for weight measurements, the influencing factors of sensor type and pavement type are fixed when installed. Thus, in this Chapter, the influences of the three major factors on the 3D-GFRP-FBG sensors for weight measurements have been studied systematically, including wheel path (vehicle maneuver), vehicle speed, and pavement temperature.

5.1. Wheel Path

The performed sensitivity in Section 4.2.3 shows that the actual wheel paths of the vehicles, which determine the loading locations on the sensor, are very important for the weight measurement accuracy. Also, since it cannot be guaranteed that the assumed wheel path location is the actual wheel path which the driver has been directed to drive on the sensor location as in a system used for LS-WIM as a part of the stationary weight scale, and it might be yield to blonder error if the system used for HS-WIM. Thus, the location of the load should be estimated and regarded as priority input of the system.

To determine the location of the load, a minimum of two sensors in the same row with known distance (H) are needed. In this study, the longitudinal component of the 3D -2 sensor and longitudinal 1D-3 sensor in the proposed sensor network will be used to detect the load locations as shown in Figure 32. The distance (H) between the two sensors was chosen to be 1 ft and 8.5 in to comply with the 1 ft. sensitivity range of the sensor as stated in Section 4.2.3. The distance of the load center is assumed to be X_1 from 1D-3 sensor and X_2 from the longitudinal component of the 3D-2 sensor. Figure 33 shows the possible loading scenario by using the two-sensor network

to determine the location of the load at the time of weighing. Figure 33 indicates that there are three loading scenarios: Scenario 1) the load is in between of the two sensors, where $X_1+X_2=H$; Scenario 2) the load is on the right of the sensor 3D-2, where $X_2=X_1-H$; Scenario 3) the load is on the left of the 1D-3 sensor, where $X_1=X_2-H$.

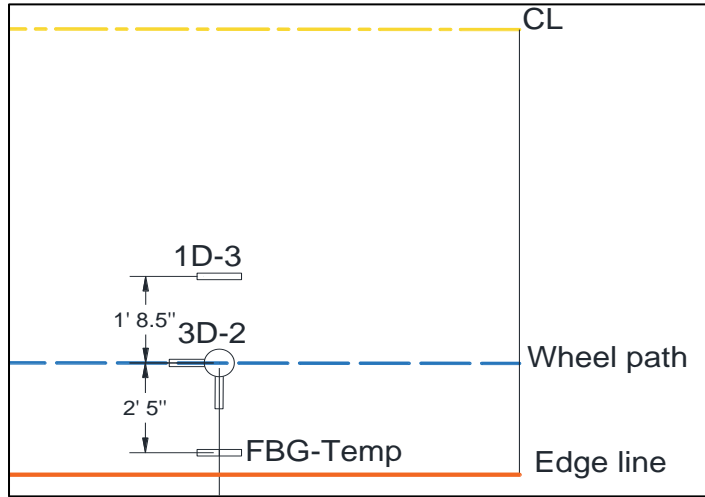


Figure 32. Sensor network to determine the loading position

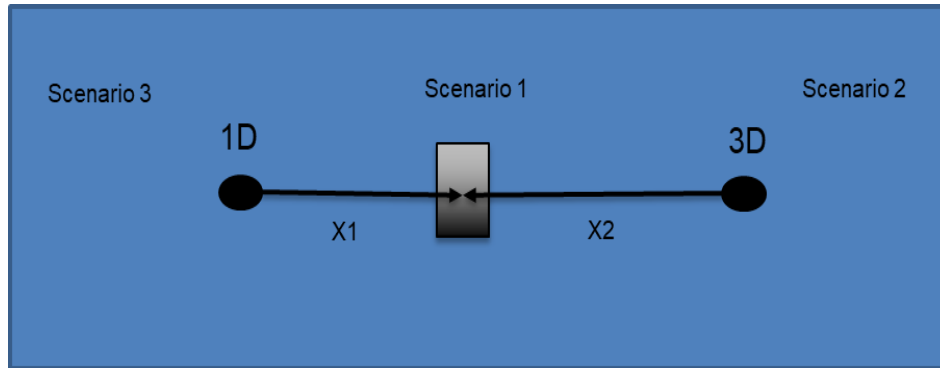


Figure 33. Loading position scenarios

In order to investigate the ability of the system to determine the location of the moving load, distances X_1 and X_2 should be estimated for all scenarios from the actual sensor response. From Equation 21, the 1D-3 sensor response (S_1) and the 3D-2 sensor longitudinal component response (S_2) can be determined as follow:

$$S_1 = \Delta\lambda_1 = P \times \lambda_1 \times \varepsilon_1 \times \phi \times (1 - P_e) \quad (25)$$

$$S_2 = \Delta\lambda_2 = P \times \lambda_2 \times \varepsilon_2 \times \phi \times (1 - P_e) \quad (26)$$

where, λ_1 and λ_2 are the center wavelengths of 1D-3 and the longitudinal part of the 3D-2 sensor, respectively, P is the measured weight, ε_1 and ε_2 are the induced strain in the host material due to the load P at sensor S_1 and sensor S_2 location, respectively, ϕ is the strain transfer rate of the GFRP to host material, and $(1 - P_e)$ is the strain sensitivity. Since the strains at the sensor's location (ε_1 and ε_2) are a function of the load location (X_1 and X_2) and the load P , and it is hard to analyze flexible pavement theoretically as shown in Equations (17-19), the KENLAYER software is used in this study to determine the strains at the sensor location.

Figure 34 shows the procedure used to calculate the actual distances X_1 and X_2 for a given load, pavement temperature, and vehicle speed with the measured strains. Estimating the pavement dynamic modulus, E^* , is a significant input to construct KENLAYER model. For a given temperature and speed, Master curve developed in Section 4.3.1 can be used to estimate E^* . Then, the given load and estimated E^* are used to construct KENLAYER model, which can be used to calculate the strain at any distance from the load and construct a strain as a function of X (load location). The strain function can be used to estimate the sensor response (S_1 and S_2) using Equations (25 and 26). Then, the actual sensors response can be used to determine X_1 and X_2 .

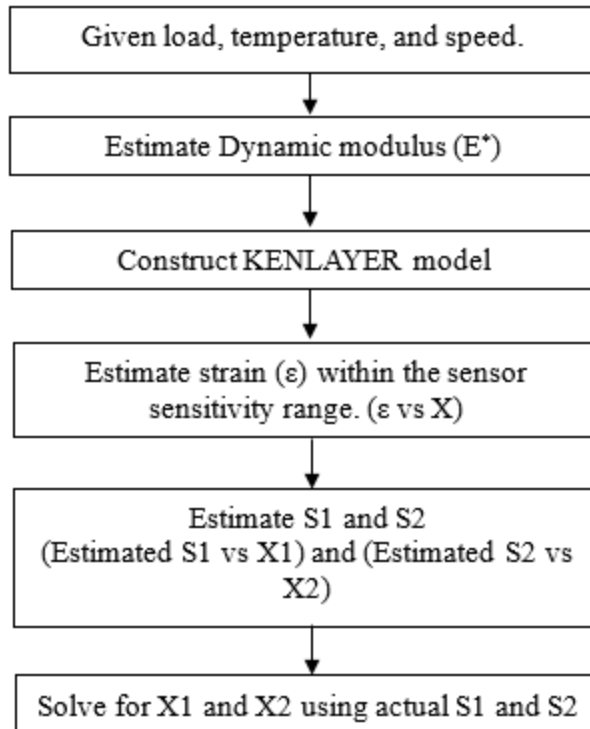


Figure 34. Loading position estimation methodology

In order to validate the system to determine the load location, a two-axle vehicle (Chevrolet Suburban) with a total gross weight of 6 Kips as shown in Figure 35 was used to generate the weight to be measured in motion. The vehicle moves three times on four different locations at 25 mph on Sep 25, 2018, to validate the system for load location determination, as shown in Figure 36. The first location (L1) is 0.75 ft. to the left of the 1D-3 sensor, the second location (L2) is just on the top of the 1D-3 sensor, the third location (L3) is just on top of the 3D-2 sensor, and the fourth location (L3) is in the middle of the distance between the 1D-3 sensor and the 3D-2 sensor.

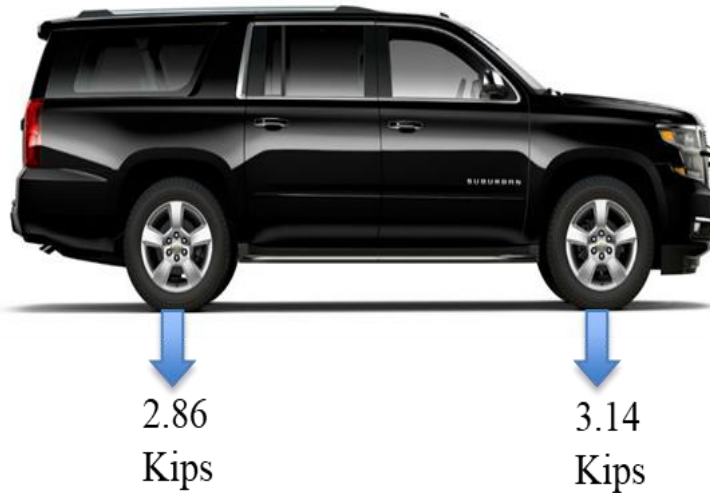


Figure 35. Vehicle load distribution

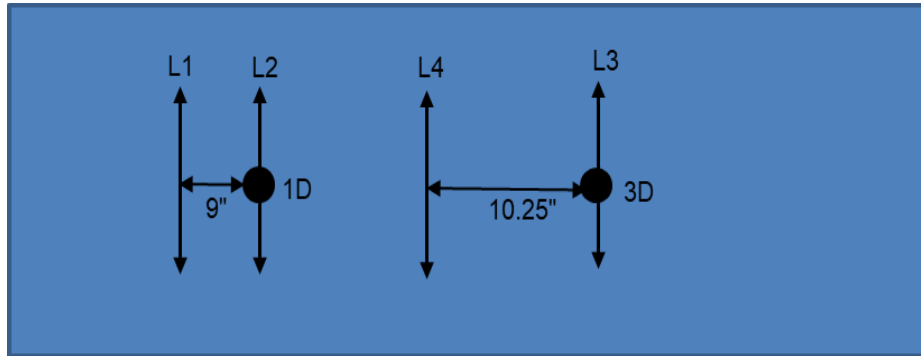


Figure 36. Loading positions

Figures (37, 38, 39, and 40) show the 3D-2 and the 1D-3 sensors' responses on locations L1, L2, L3, and L4, respectively. Figures (37, 38) indicates that on locations L1 and L2 since the vehicle runs near to the 1D-3 sensor, it is obvious that the 1D-3 sensor's response is much higher than that of the 3D-2 sensor. Figure 38 shows that the 3D-2 sensor is still sensitive to the load when the load is on location L2, but it seems that the 3D-2 sensor's response is not sensitive to the load when the vehicle is passed on location L1, which complies with the simulation results of the performed sensitivity study in Section 4.3.2. Conversely, as shown in Figure (39) on location L3, the vehicle is supposed to move on top of the 3D-2 sensor. Therefore, the 3D-2 sensor has a higher sensor response, but the 1D-3 sensor is still sensitive to the load. Figure 40 shows that both sensors'

responses (1D and 3D) on Location L4, which lays in between sensors 1D-3 and 3D-2. It clearly indicates that the load is moved in between the 1D-3 sensor and the 3D-2 sensor since the response is approximately identical. Both sensors show high repeatability accuracy in all three runs, as shown in Figures (37, 38, 39, and 40).

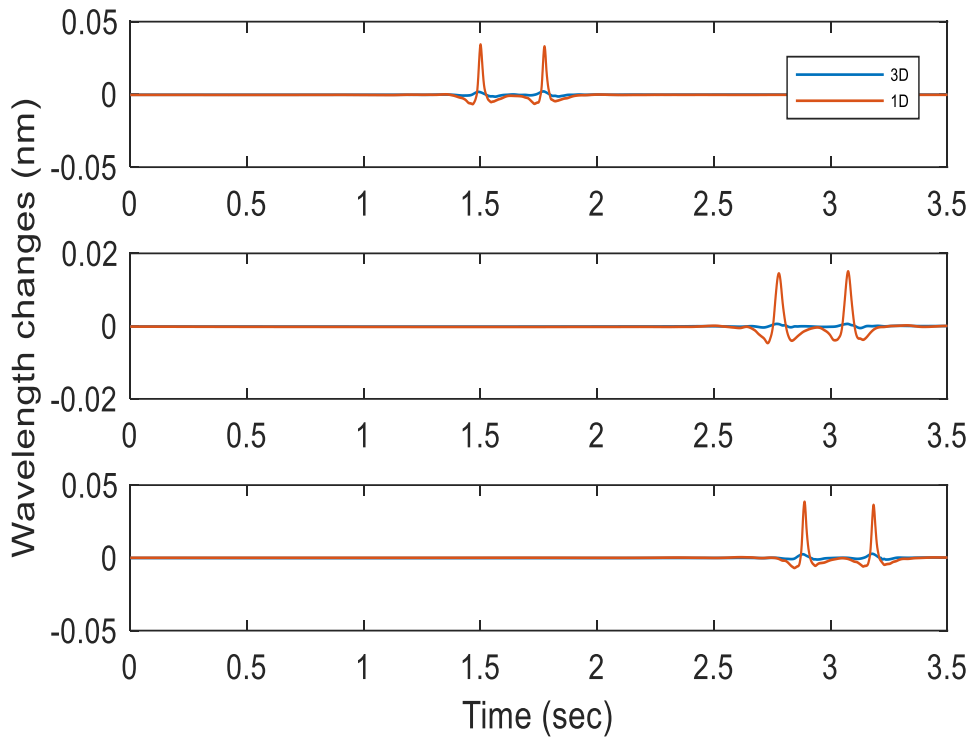


Figure 37. 3D-2 and 1D-3 sensors' responses for three runs using loading position L1

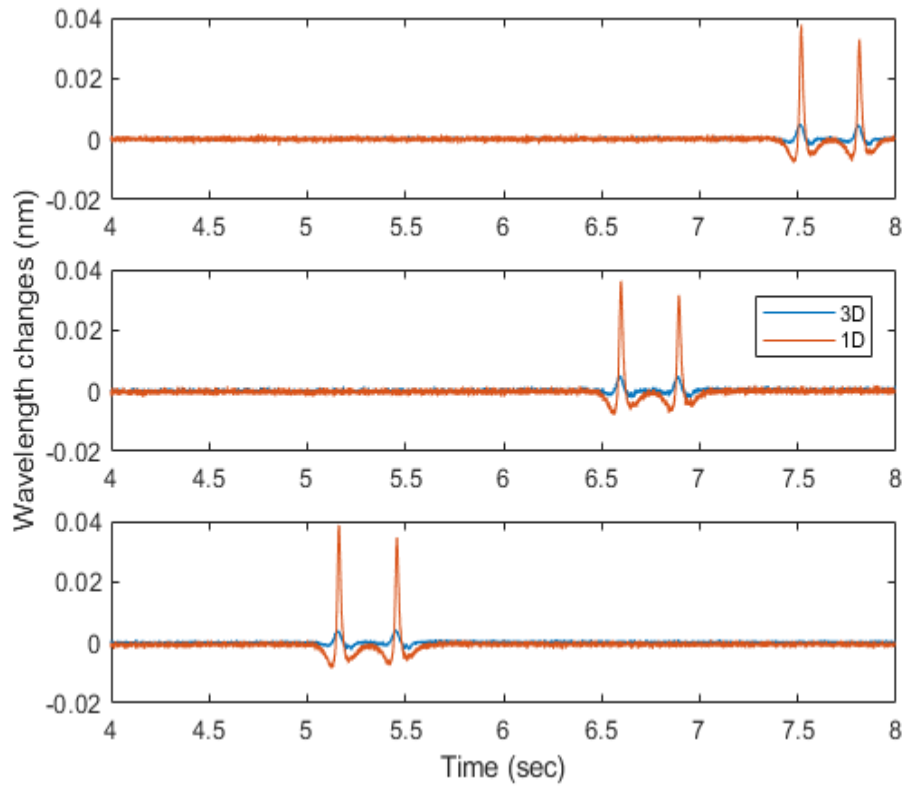


Figure 38. 3D-2 and 1D-3 sensors' responses for three runs using loading position L2

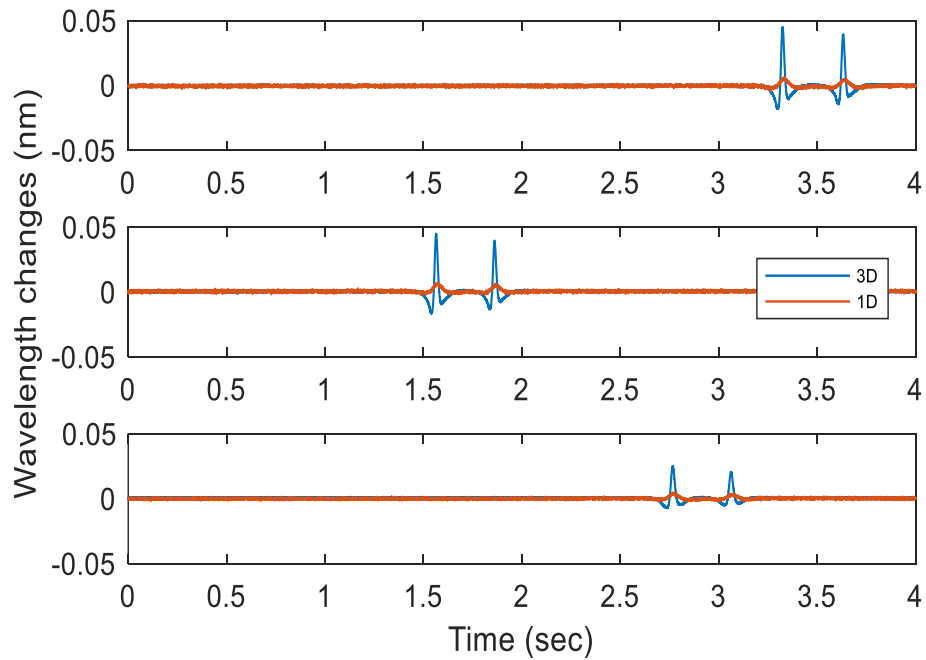


Figure 39. 3D-2 and 1D-3 sensors' responses for three runs using loading position L3

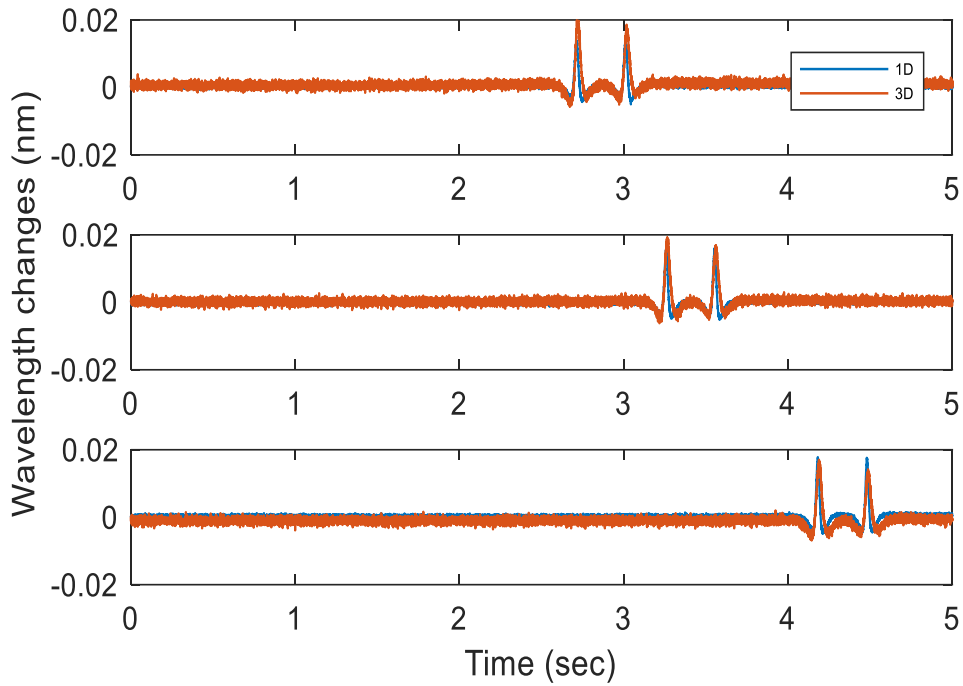


Figure 40. 3D-2 and 1D-3 sensors' responses for three runs using loading position L4

Figure 41 shows the simulated sensor's response (S1 and S2) with the load location (X) for tow axle's right tire of the vehicle passing on location L4. The first axle's right tire weights 1.57 Kips and the second axle's right tire weights 1.43 Kips. In order to construct the sensor response function, the temperature was monitored by a FBG temperature compensation sensor, and the recorded temperature was 17.9 C°. The speed was recorded using the radar gun, and it was 25 mph. The temperature and the speed were used to estimate the dynamic modulus of the pavement, which resulted in a dynamic modulus of 1678.9 ksi for the pavement. The first run of the vehicle has an actual sensor response for 1D-3 sensor equals to 0.0152 nm and for 3D-2 sensor equals to 0.0192 nm for the first axle's tire. Following the procedure in Figure 34 and the simulated sensor response in Figure 41, the value of X1 and X2 was determined to be 11.6 in. and 8.9 in., respectively.

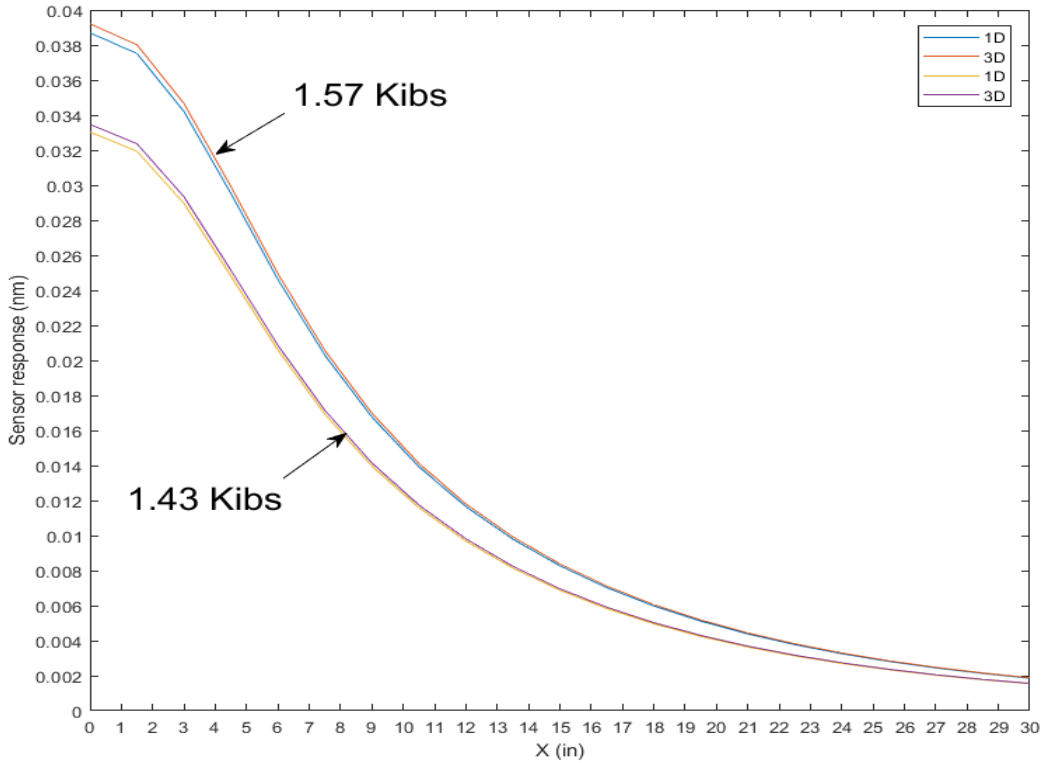


Figure 41. Sensor's response changes with load location

In order to investigate the effect of the load location on the weighing measurements, the weights were measured on all locations (L1, L2, L3, and L4) based on the assumed location in Figure 35 following the proposed procedure in Chapter 4.

Furthermore, those results are compared with the measured weights using the estimated load locations from the measured results. Table 13 summarizes the input of KENLAYER model for all locations. Table 14 summarizes the WIM measurements from the longitudinal component of the 3D-2 sensor and the 1D-3 sensor for each vehicle axle for all locations before eliminating the load location effect for one run. When compared with the reference weights which are the actual weights of the vehicle axle, both sensors show measurements inaccuracy greater than the acceptable range of 10% error, and that due to the variance of loading position for each axle different than the assumed positions.

Table 13. KENLAYER model input for all loading positions

Location	Speed (mph)	Temperature(C°)	E*(Ksi)
L1	25	16.46	1795.1
L2		16.46	1795.1
L3		17.08	1747.2
L4		17.96	1678.9

Table 14. WIM measurements error using the assumed loading positions

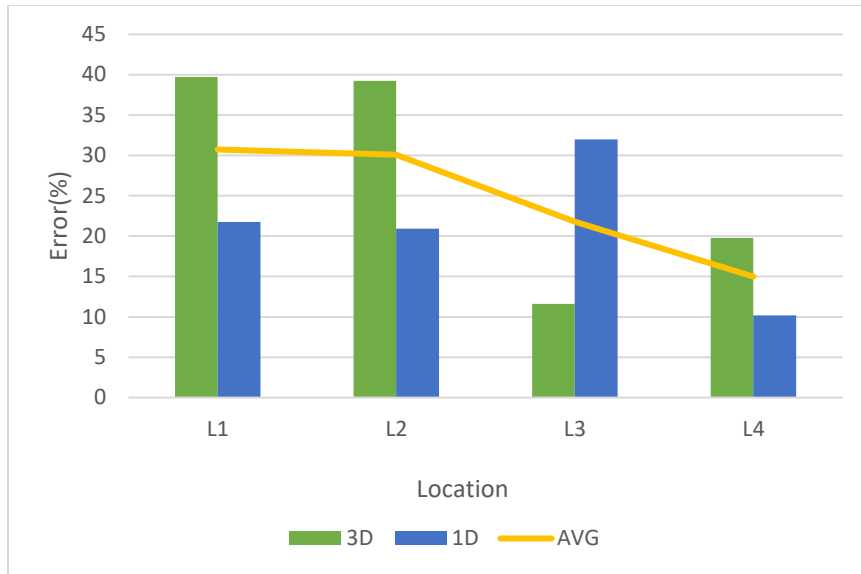
Reference weight		Axle 1		Axle 2	
		1.57 kips		1.43 kips	
Location		3D	1D	3D	1D
L1	Wavelength changes (pm)	2.45	23	2.8	20.7
	WIM (kips)	1.95	2.15	2.45	2.12
	Error (%)	24.5	37.3	71.4	48.4
L2	Wavelength changes (pm)	7.3	44.9	6	39.7
	WIM (kips)	2.45	1.82	2.21	1.72
	Error (%)	56.2	16	54.7	20.2
L3	Wavelength changes (pm)	45	6.3	34.7	6
	WIM (kips)	1.76	2.14	1.66	2.24
	Error (%)	12.7	36.4	16.5	56.5
L4	Wavelength changes (pm)	17	17.8	16.9	16.1
	WIM (kips)	1.72	1.82	1.83	1.76
	Error (%)	9.3	15.9	16.4	12.4

To validate the proposed vehicle location error correction methodology for enhancing the weighing measurements accuracy, Table 15 summarizes the weight measurement for the same loading positions and the same run which summarized in Table 14 after correction on loading positions. It can be clearly seen that the correcting loading positions significantly reduces the inaccuracy of the measurement. The average measurements error for all loading positions (L1, L2, L3, and L4) based on Table 14 are 45.4%, 36.8%, 30.5%, and 13.5% before applying the proposed methodology, respectively. The measurements inaccuracies for all loading positions (L1, L2, L3, and L4) are 6.1%, 5.4%, 5.7%, and 2.9% after loading position corrections, which are all fall in the allowable range less than 10% on average.

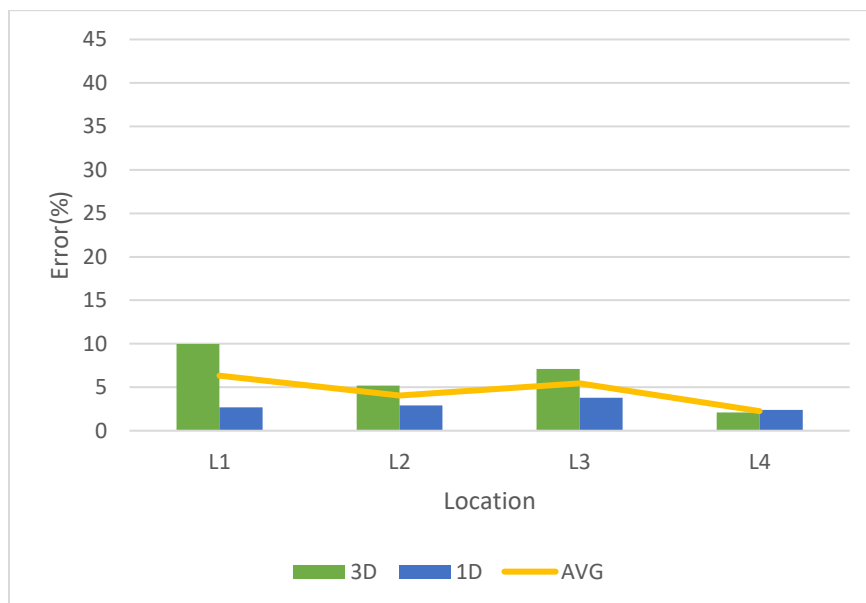
Table 15. WIM measurements error using the estimated loading positions

Reference weight		Axle 1		Axle 2	
		1.57 kips		1.43 kips	
Location		3D	1D	3D	1D
L1	Wavelength changes	2.45	23	2.8	20.7
	WIM (kips)	1.41	1.65	1.46	
	Error (%)	10.2	5.6	2.4	6.2
L2	Wavelength changes	7.3	44.9	6	39.7
	WIM (kips)	1.49	1.71	1.48	1.36
	Error (%)	4.7	8.9	3.7	4.4
L3	Wavelength changes	45	6.3	34.7	6
	WIM (kips)	1.69	1.68	1.52	1.44
	Error (%)	7.6	7.3	6.8	1.2
L4	Wavelength changes	17	17.8	16.9	16.1
	WIM (kips)	1.61	1.63	1.47	1.46
	Error (%)	2.5	3.5	3.2	2.4

Since the vehicle moves on each loading position three times, Figure 42 (a) summarized the inaccuracy of the measurements for each loading position before loading position correction, and Figure 42 (b) shows the measurements error after applying the proposed correction methodology. From Figure 42, it can be concluded that the proposed loading position correction methodology significantly reduces the measurements inaccuracy to allowable limit less than 10% and eliminate the error variances among the two sensors since the sensors have a big variance in error measurements as shown in Figure 42 (a). In contrast, Figure 42 (b) shows that both sensors have less variances in error measurements.



(a)



(b)

Figure 42. Weight measurement error for all loading positions (L1, L2, L3, and L4) using assumed loading positions (a) and using corrected loading positions (b)

5.2. Vehicle Speed

Since the sensor network is installed in the flexible pavement (a visco-elastic material), which means that the modulus of elasticity of the material changes with the load frequency. Based

on Equation (24), the loading frequency is a function of the vehicle speed (v). Figure 43 shows the changes in the pavement dynamic modulus (E^*) with a vehicle speed at a fixed pavement material temperature. From Figure 43, it can be seen that if the vehicle speed is increased from 10 mph to 20 mph, the dynamic modulus will be increased by 15% approximately. Also, based on the sensitivity study performed in Section 4.2.3, the dynamic modulus is significantly affecting the WIM measurements sensitivity. Thus, the vehicle speed is expected to influence the WIM measurements sensitivity of the developed system.

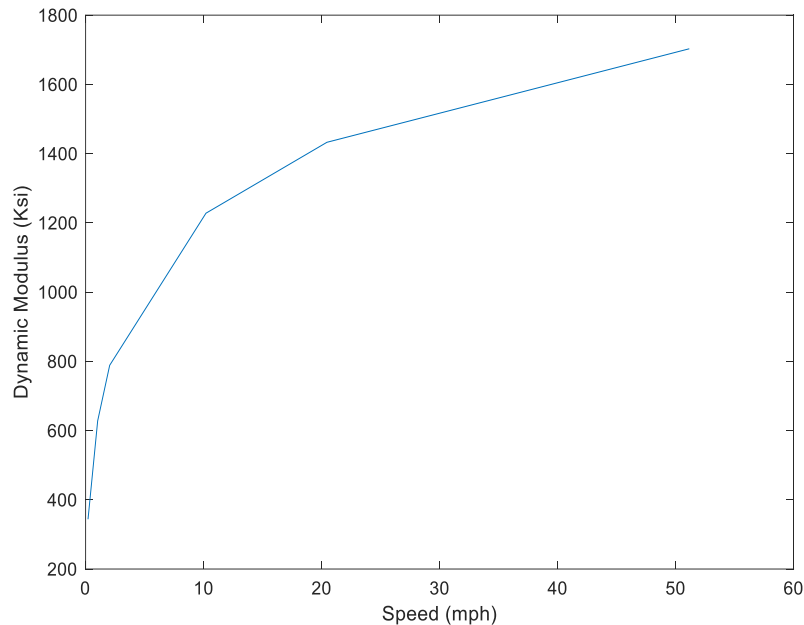


Figure 43. Dynamic modulus (E^*) changes with vehicle speed

Figure 44 shows the change of the WIM sensitivity with different vehicle driving speeds. The WIM sensitivity is noticed to significantly decrease in the low-speed range from 1 mph to 25 mph, after 25 mph the WIM sensitivity still decrease but with less effect.

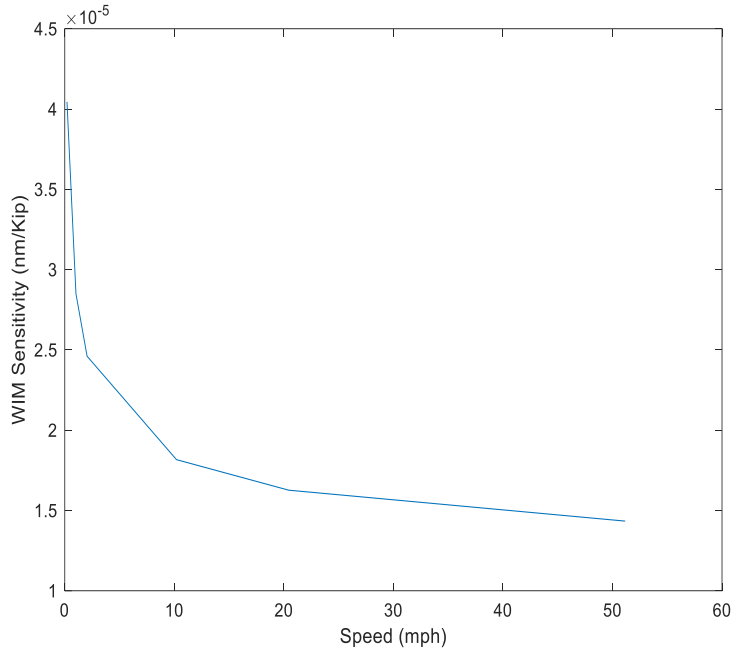


Figure 44. WIM sensitivity changes with vehicle speed

To distinguish the vehicle speed effects from the influence of pavement temperature and loading position on the weighing error, the vehicle moves on the top of the 3D-2 sensor using loading position (L3) three times at five different speeds of 10 mph, 20 mph, 30 mph, 40 mph, and 50 mph at a recorded temperature of 14.8 C°. Figures (45, 46, 47, 48, and 49) show the 3D-2 sensor responses on its longitudinal component and the 1D-3 sensor responses at 10 mph, 20 mph, 30 mph, 40 mph, and 50 mph vehicle speed, respectively. Table 16 summarizes the estimated dynamic modulus for each vehicle speed, which will be used as the input of KENLAYER model.

Table 16. KENLAYER model input at a different vehicle speed

Speed (mph)	Location	Temperature(C°)	E*(Ksi)
10	L3	14.8	1663.4
20			1861.8
30			1973.1
40			2049.4
50			2106.9

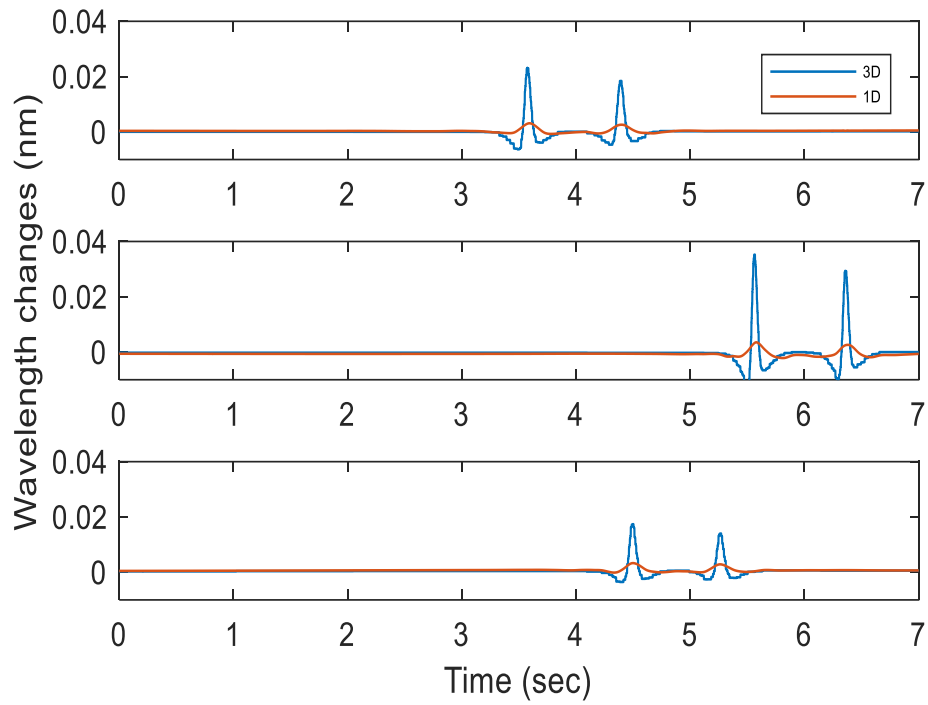


Figure 45. 3D-2 and 1D-3 sensors' response at 10 mph vehicle speed

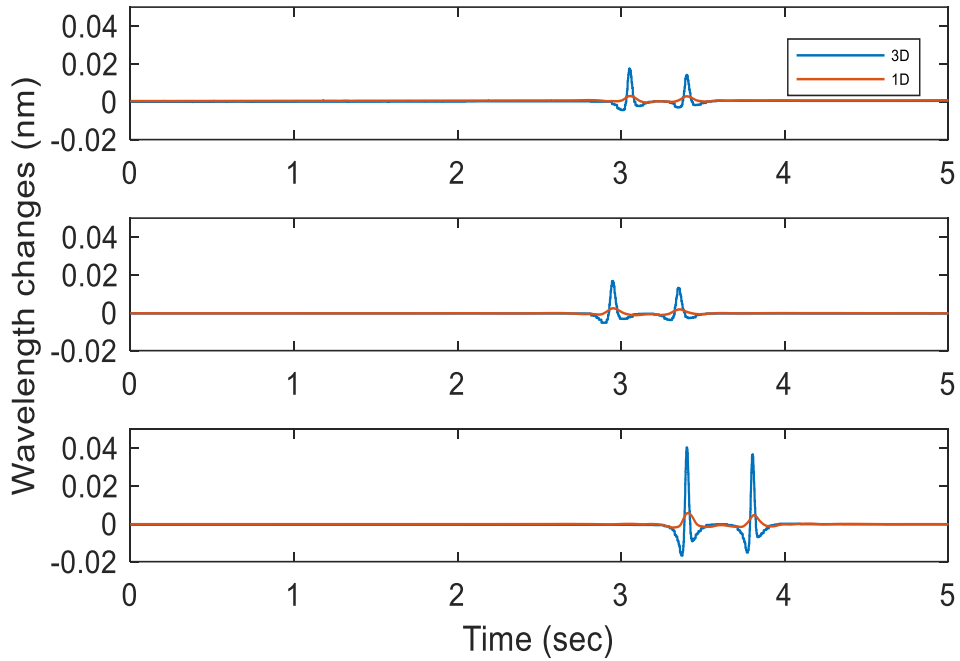


Figure 46. 3D-2 and 1D-3 sensors' response at 20 mph vehicle speed

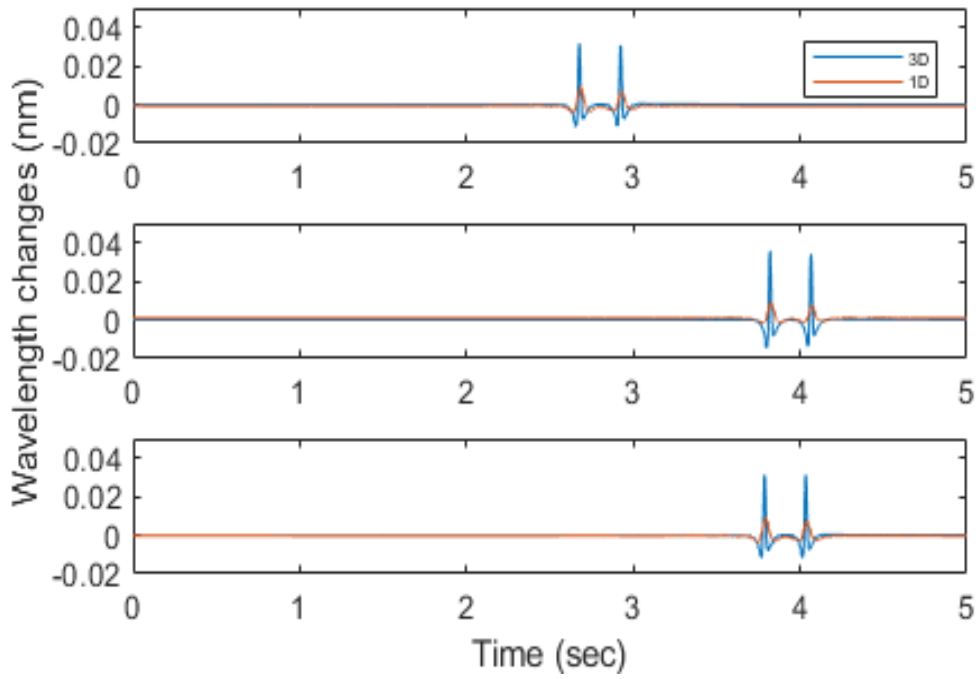


Figure 47. 3D-2 and 1D-3 sensors' response at 30 mph vehicle speed

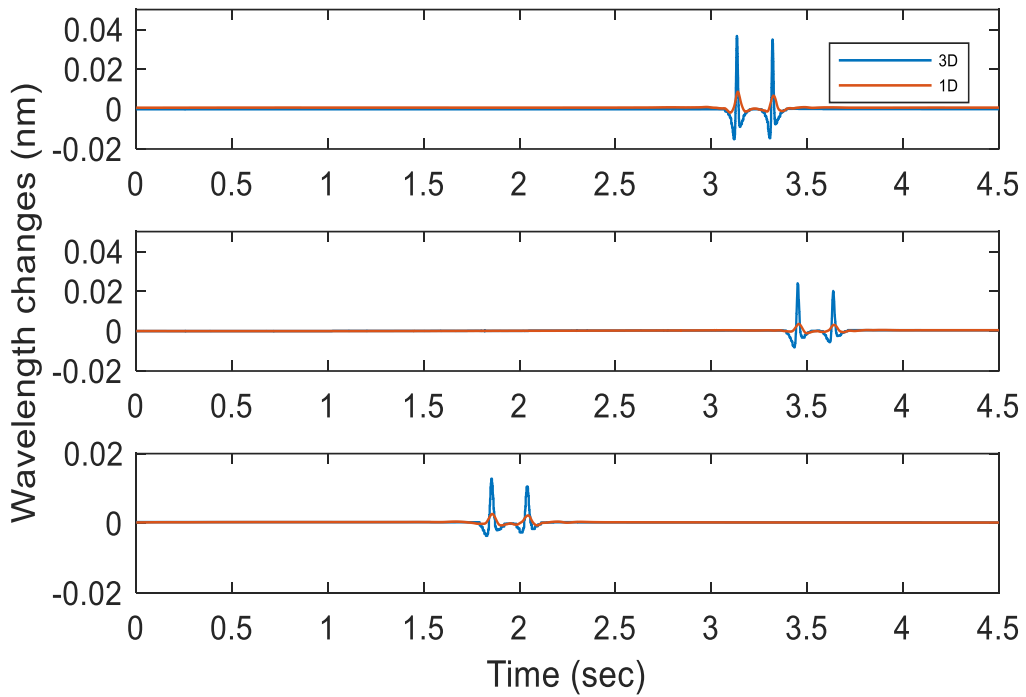


Figure 48. 3D-2 and 1D-3 sensors' response at 40 mph vehicle speed

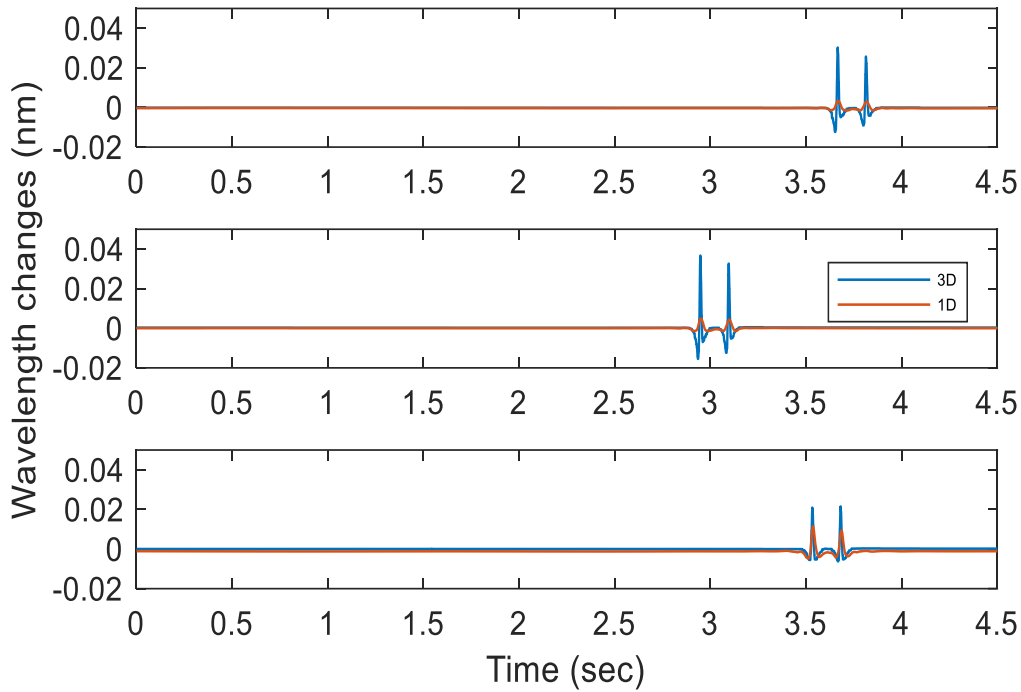
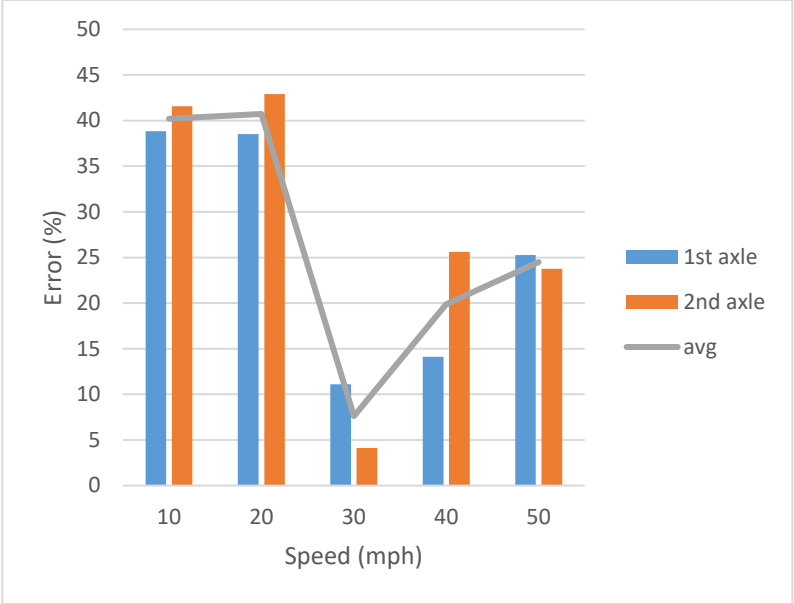
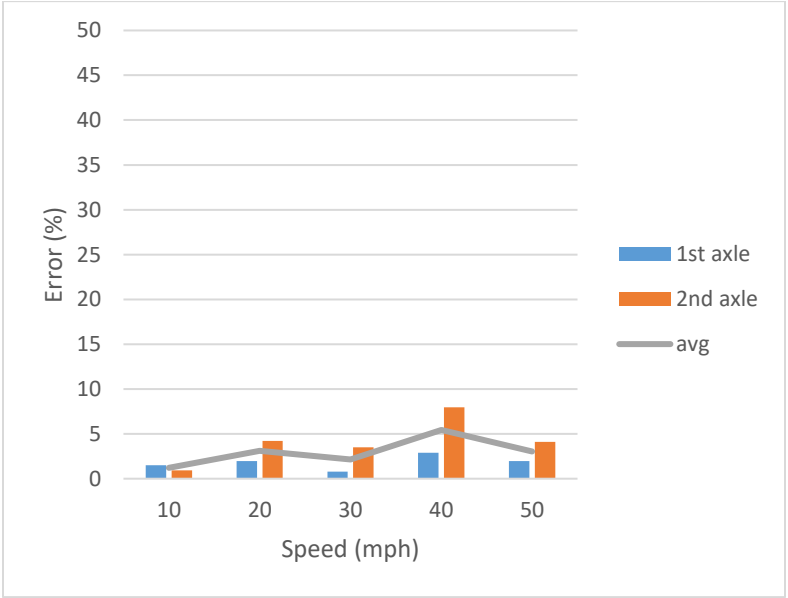


Figure 49. 3D-2 and 1D-3 sensors' response at 50 mph vehicle speed

Figure 50 (a) shows the calculated weighing error based on the assumed loading position using the 3D-2 sensor longitudinal component. The 3D-2 sensor has high inaccuracy greater than 30% on average for all vehicle speed. This blonder error is a result of loading and speed together. To eliminate the effect of loading position on the weight measurements, the methodology in Section 5.1 is used, and the weighing error is calculated based on the corrected loading position as shown in Figure 50 (b). Figure 50 (b) indicates that the inaccuracy in WIM measurements decreased significantly less than 10% on average for all vehicle speed. Comparing the results from Figure 50 (b) to the results from Figure 50 (a), the loading position is still the major parameter affecting the WIM measurements accuracy followed by the vehicle speed. The effect of vehicle speed on the WIM measurements accuracy can be eliminated by using a high sampling frequency of the integrator and a good estimate of the pavement dynamic modulus.



(a)



(b)

Figure 50. Weight measurements error at vehicle speed (10, 20, 30, 40, and 50) mph using assumed loading position (a) and using corrected loading position(b)

5.3. Host Material Temperature

Section 4.1.3. shows the dependency of the flexible pavement dynamic modulus (E^*) on the pavement temperature, due to the large variance between day and night temperature. Hence,

the pavement temperature effect on the accuracy of the WIM measurements should be evaluated.

Figure 51 shows the changes in the dynamic modulus (E^*) with the pavement temperatures. As the pavement temperature increased the dynamic modulus decreased, which yields to increase the WIM measurements sensitivity, as shown in Figure 52.

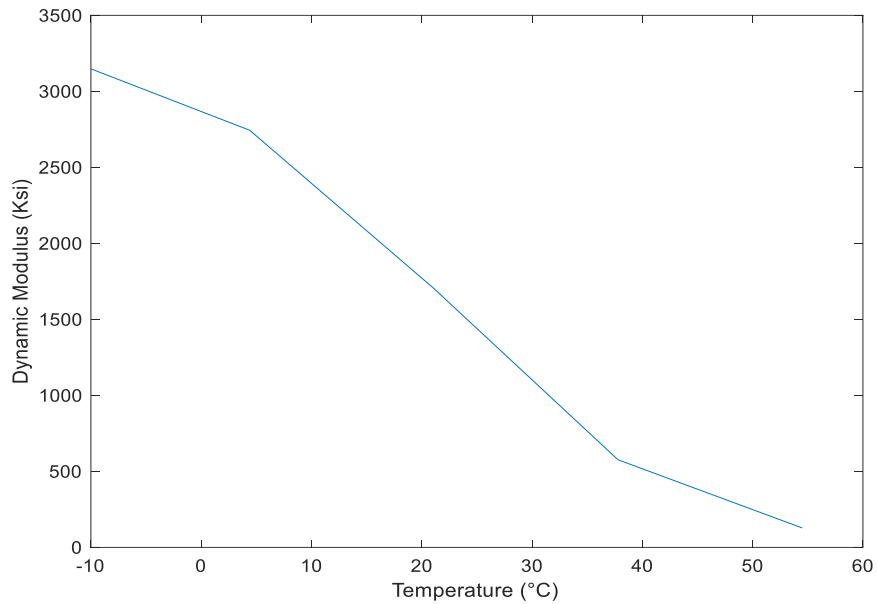


Figure 51. Dynamic modulus changes with pavement temperature

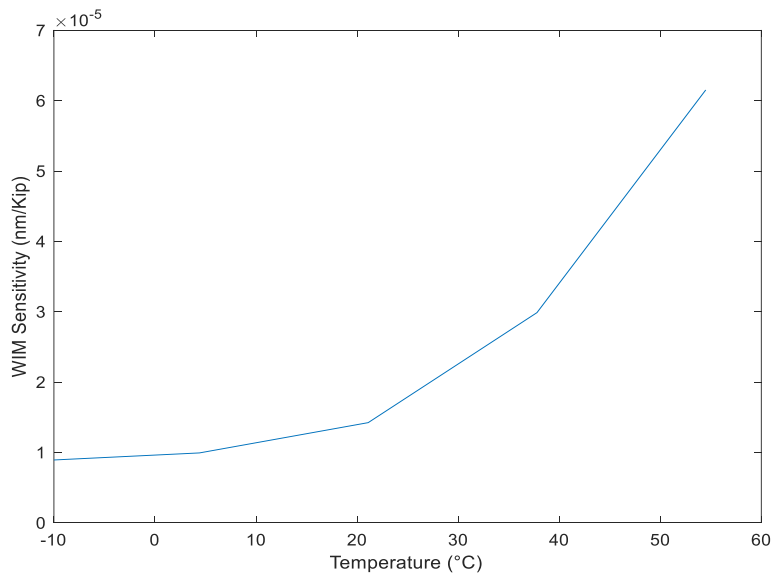


Figure 52. WIM measurements sensitivity changes with pavement temperature

To distinguish the pavement temperature effect from the influence of vehicle speed and the loading position on the weighing error, the vehicle moves on the top of the 3D sensor using loading position (L3) three times at three different periods on 9/25/2018 at 25 mph vehicle speed. The pavement temperature was monitored using the FBG temperature compensation sensor for the three different periods, and recorded as follow 14.6 C°, 17.1 C°, and 19.9 C° for the morning, noon, and afternoon periods, respectively. Figure 53 shows the 3D-2 sensor's responses and the 1D-3 sensor's responses at 25 mph vehicle speed in the noon period with a recorded temperature of 17.1 C°. Table 17 summarizes the estimated dynamic modulus for each recorded temperatures, which were used as the input of KENLAYER model.

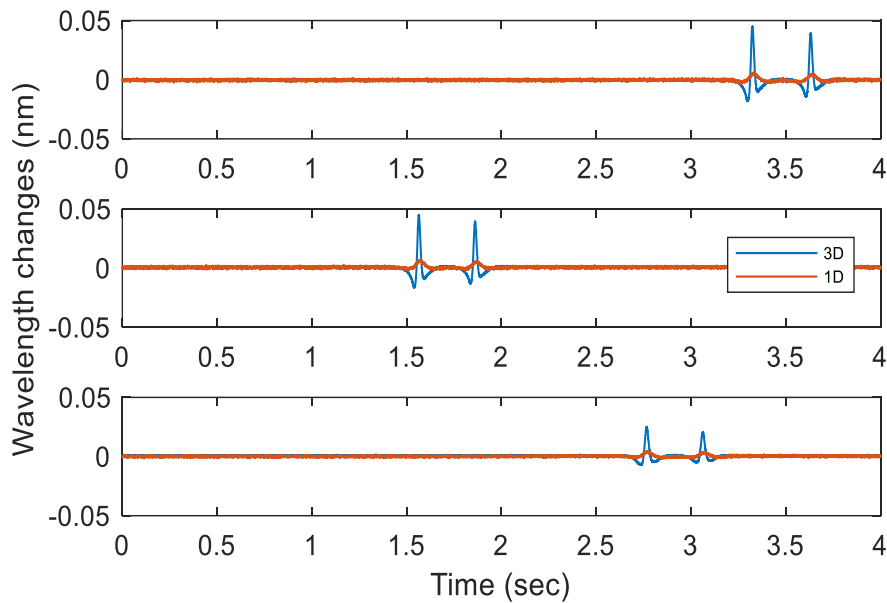


Figure 53. 3D and 1D sensor's response at 17.1 °C pavement temperature

Table 17. KENLAYER model input at different pavement temperature

Temperature(C°)	Location	Speed (mph)	E*(Ksi)
14.6	L3	25	1940.1
17.1			1747.2
19.9			1521.6

Figure 54 shows the average calculated weighing error for all vehicle runs based on the assumed loading position using the 3D sensor longitudinal component (Avg-B) and based on the corrected loading position (Avg-A). From Figure 54, it is obvious that the effect of pavement temperature on the weighing error is less significant compared with the effect of the loading position. Besides, the average error is within 10% allowable range after eliminating the load position effect.

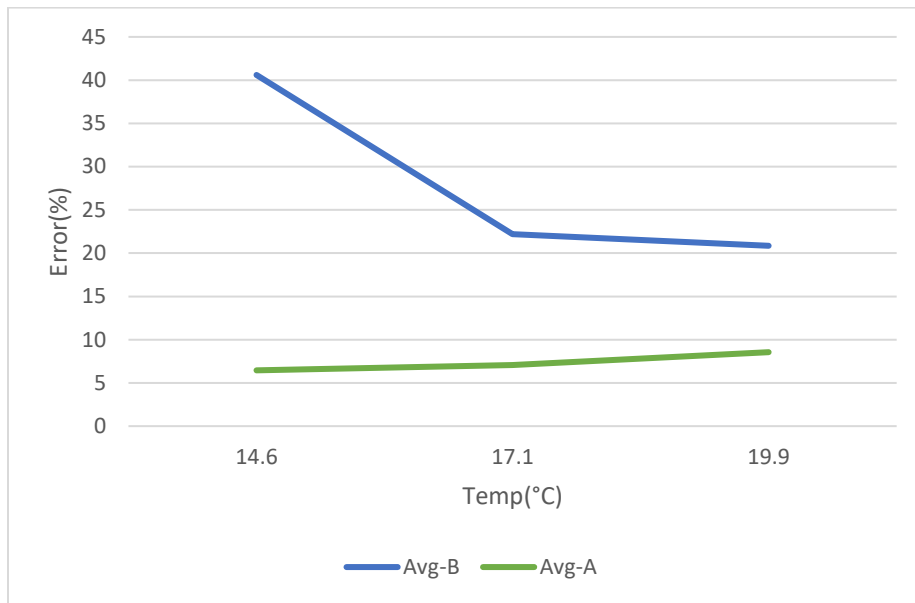


Figure 54. Weight measurements error at pavement temperature (14.6, 17.1, and 19.9) °C using assumed loading position (Avg-B) and using corrected loading position (Avg-A)

5.4. Traffic Monitoring System

Based on the findings in this study, a cost-effective comprehensive traffic monitoring system can be constructed using the proposed GFRP-FBG sensors in order to extract all the parameters that describe the characteristics of vehicles and their movement on the road. In this section, a sensor network based on the FBG sensor is introduced for two-lane highway with a typical lane width of 12 ft. Since the longitudinal component of the GFR- FBG sensor has the better performance among other components, a nine 1D-GFRP-FBG sensor (in longitudinal

direction) will be installed at the bottom of the pavement wearing layer in one row with 2.4 ft. of distance between each other. This will guarantee the detection of all rolling axles and comply with the proposed methodology in Section 5.1 to precisely estimate the loading position for weighing purposes as shown in Figure 55. Also, a two 1D GFRP-FBG sensor (in the longitudinal direction) will be used at 16 ft distance from the longitudinal sensor row for speed, wheelbase, and vehicle class estimation. In order to monitor the pavement temperature, three FBG temperature compensation sensors will be used, as shown in Figure 55. Also, a weather station will be installed on the roadside to monitor other weather conditions such as moisture, humidity, etc.

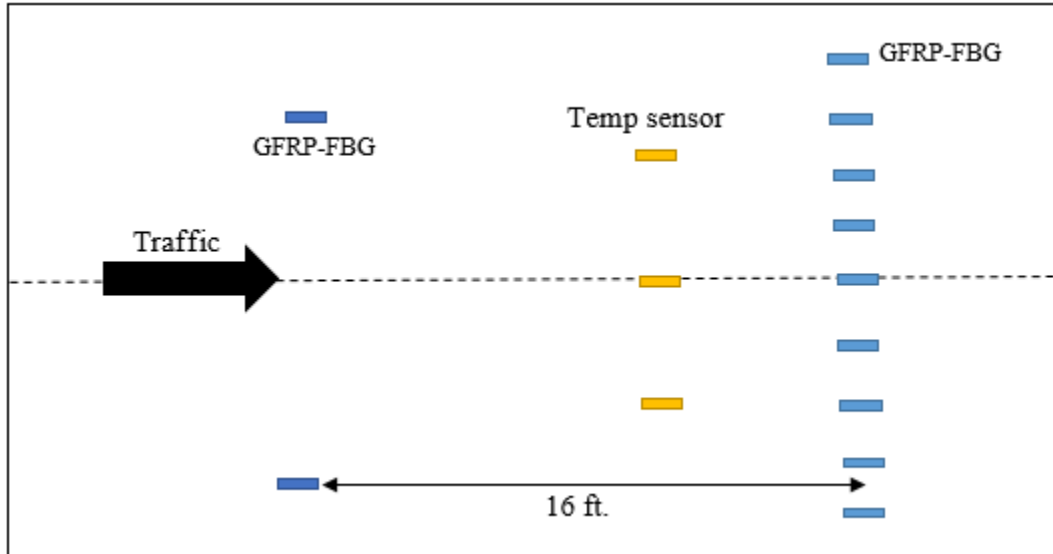


Figure 55. Traffic monitoring system

In order to monitor the traffic in real time, a multi-channel wireless integrator with high sampling frequency up to 20 KHz will be used. This integrator will be connected with a storage device which has the ability to reach the internet. The cost of the proposed system can be estimated as follows: \$1100 for all GFRP-FBG sensors, \$150 for FBG temperature compensation sensors, \$250 for cables, \$4500 for the wireless integrator, \$500 for the storage device, and \$3500 for the weather station. The approximate cost for the proposed system is within \$10,000.

6. CONCLUSION AND FUTURE WORKS

This study introduced a traffic monitoring system based on GFRP-FBG sensors which can be installed inside flexible pavements. The conclusions of this study can be drawn as follows:

- 1) The proposed system can survive the harsh construction process of pavement construction and extract various vehicle parameters including vehicle speed, wheelbase distances, and number of axles;
- 2) The system can accurately estimate the speed and the wheelbase, with an accuracy above 98%;
- 3) The field-testing results from real traffic show that the developed system can classify vehicle very accurately and using SVM-OAO and NN classifier have slightly higher accuracy than KNN and SVM-OAA. SVM-OAO and NN based classification system has an average accuracy of 97.5%, followed by SVM-OAA and KNN with an average accuracy of 96 %;
- 4) The system can successfully perform counting of axles and vehicles by tracking the peaks through the sensor's response;
- 5) For WIM measurements, the GFRP-FBG sensor is very sensitive to the sensor installation depth, the modulus of the embedded host materials, and location of the loading. The best performance for WIM measurements is to install the sensor at the bottom of the pavement sections, the sensor's WIM measurement sensitivity will decrease with the increase of the modulus of the embedded host materials, and the WIM sensitivity of all sensor's components tends to zero after one foot;
- 6) For WIM measurements, field testing validated that the longitudinal component of the sensor without any corrections has a measurement accuracy of 86.3% and 89.5% at 5

mph and 45 mph vehicle speed, respectively. However, the performed parametric study on the stability of WIM system shows that the loading position is the most significant parameter affecting the WIM measurements accuracy in addition to the vehicle speed and pavement temperature. With the correction in loading locations, the WIM measurements error can be lowered to the allowable limit of 10%.

In the future, efforts will continue to transform the current wired sensing system into a wireless system using Internet of-Thing (IoT). Also, other influencing factors measured from weather station such as moisture, wind, etc. will be considered in the future.

REFERENCES

- [1] Bajwa RS. Wireless Weigh-In-Motion: using road vibrations to estimate truck weights. University of California, Berkeley; 2013.
- [2] Fernando EG, Middleton D, Carlson TB, Longmire R, Sepulveda ED, Ruback LG, Freeman TJ, Oh J. Deploying Weigh-in-motion Installations on Asphalt Concrete Pavements. No. FHWA/TX-09/0-5551-1. 2009 Feb.
- [3] Jacob B, Feypell-de La Beaumelle V. Improving truck safety: Potential of weigh-in-motion technology. IATSS research. 2010 Jul 31, 34(1):9-15.
- [4] Taylor B, Bergan A, Lindgren N, Eng CB. The importance of commercial vehicle weight enforcement in safety and road asset management. Annual Review pp. 2000 Jan, 234:237.
- [5] Jinwoo Brian LE, Hanseon CH. Commercial Vehicle Preclearance Program: Motor Carriers' Perceived Impacts and Attitudes towards Potential Implementation. In Proceedings of the Eastern Asia Society for Transportation Studies 2013 (Vol. 9).
- [6] Karim MR, Ibrahim NI, Saifizul AA, Yamanaka H. Effectiveness of vehicle weight enforcement in a developing country using weigh-in-motion sorting system considering vehicle by-pass and enforcement capability. IATSS research. 2014 Mar 1;37(2):124-9.
- [7] Dey KC, Chowdhury M, Wiecek MM, Dunning A. Infrastructure damage-cost-recovery fee for overweight trucks: Tradeoff analysis framework. Journal of Transportation Engineering. 2015 Mar 12;141(7):04015008.
- [8] Al-Qadi I, Ouyang Y, Wang H, Meidani H, Gungor OE, Petit A, Zhao J, Qiu J. Development of Overweight Vehicle Permit Fee Structure in Illinois. Illinois Center for Transportation/Illinois Department of Transportation; 2017.

- [9] Szary PJ, Maher A. Implementation of Weigh-in-motion (WIM) Systems. No. FHWA-NJ-2009-001. 2009 Feb.
- [10] Robert FL, Kandhal PS, Brown ER, Lee DY, Kennedy TW, Hot Mix Asphalt Materials, Mixture Design, and Construction, NAPA Education Foundation, Second Edition, Lanham, Maryland, 1996.
- [11] Schrank D, Eisele B, Lomax T. 2014 Urban mobility report: powered by INRIX Traffic Data. 2015 Jul.
- [12] Federal Highway Administration (FHWA). Traffic Monitoring Guide. 2013.
- [13] Mimbela LEY, Klein LA. Summary of Vehicle Detection and Surveillance Technologies Used in Intelligent Transportation Systems. 2000 [cited 2018 Mar 12]. Available from: <https://www.fhwa.dot.gov/ohim/tvtw/vdstits.pdf>
- [14] Michalopoulos PG. Vehicle detection video through image processing: the autoscope system. IEEE Transactions on vehicular technology. 1991 Feb;40(1):21-9.
- [15] Nooralahiyan AY, Kirby HR, McKeown D. Vehicle classification by acoustic signature. Mathematical and Computer Modelling. 1998 May 1;27(9-11):205-14.
- [16] Arora A, Dutta P, Bapat S, Kulathumani V, Zhang H, Naik V, Mittal V, Cao H, Demirbas M, Gouda M, Choi YR. A line in the sand: a wireless sensor network for target detection, classification, and tracking. Computer Networks. 2004 Dec 5;46(5):605-34.
- [17] Garcia F, Cerri P, Broggi A, Armingol JM, De La Escalera A. Vehicle detection based on laser radar. In International Conference on Computer Aided Systems Theory 2009 Feb 15 (pp. 391-397). Springer, Berlin, Heidelberg.

- [18] Ki YK, Baik DK. Vehicle-classification algorithm for single-loop detectors using neural networks. *IEEE Trans Veh Technol.* 2006;55(6):1704–11.
- [19] Sun C, Ritchie SG, Oh S. Inductive classifying artificial network for vehicle type categorization. *Computer-Aided Civil and Infrastructure Engineering.* 2003 May 1;18(3):161-72.
- [20] Cheung S, Coleri S, Dundar B, Ganesh S, Tan C-W, Varaiya P. Traffic Measurement and Vehicle Classification with Single Magnetic Sensor. *Transp Res Rec.* 2005;1917(January):173–81.
- [21] Cheung S. Traffic Surveillance by Wireless Sensor Networks: Final Report. *Calif Path Progr Inst Transp Stud Univ California, Berkeley.* 2007;1(January):161.
- [22] Peters B, Koniditsiotis C. Weigh-In-Motion Technology. (ISBN085588553X) Austroads project No. RUM. TM. 2000, 9.
- [23] Liu R, Chen X, Li J, Guo L, Yu J. Evaluating Innovative Sensors and Techniques for Measuring Traffic Loads. Final Project Report, *TxDOT Project 0-4509.* 2006 Oct.
- [24] U.S. Department of Transportation, Federal Highway Administration, Office of Freight Management Operations, *Freight Analysis, version 3, 2010.*
- [25] Wierzba P, Kosmowski B. Polarimetric sensors for weigh-in-motion of road vehicles. *Optoelectron Rev.* 2000;8(2):181–7.
- [26] ASTM Standard E1318-02, Highway Weigh-in-Motion (WIM) Systems with User Requirements and Test Methods, *Annual Book of ASTM Standards, 2002.*
- [27] Bushman R, Pratt AJ. Weigh in motion technology–economics and performance. In *Presentation on the North American Travel Monitoring Exhibition and Conference (NATMEC).* Charlotte, North Carolina 1998 May.

- [28] Weigh-in-Motion [Internet]. [cited 2019 Apr 9]. Available from:
<https://www.pavementinteractive.org/reference-desk/design/design-parameters/weigh-in-motion/>.
- [29] Martin PT, Feng Y, Wang X. Detector technology evaluation. Fargo, ND: Mountain-Plains Consortium; 2003 Nov.
- [30] Lee B. Review of the present status of optical fiber sensors. *Optical fiber technology*. 2003 Apr 1;9(2):57-79.
- [31] Majumder M, Gangopadhyay TK, Chakraborty AK, Dasgupta K, Bhattacharya DK. Fibre Bragg gratings in structural health monitoring-Present status and applications. *Sensors Actuators, A Phys*. 2008;147(1):150–64.
- [32] Zhang L, Haas C, Tighe SL. Evaluating Weigh-In-Motion Sensing Technology for Traffic Data Collection. *Transportation Association of Canada*. 2007;1–17.
- [33] Mendez A. Fiber Bragg grating sensors: a market overview. In *Third European Workshop on Optical Fibre Sensors 2007 Jul 2* (Vol. 6619, p. 661905). International Society for Optics and Photonics.
- [34] Malla RB, Sen A, Garrick NW. A special fiber optic sensor for measuring wheel loads of vehicles on highways. *Sensors*. 2008 Apr 11;8(4):2551-68.
- [35] Hill KO, Meltz G. Fiber Bragg grating technology fundamentals and overview. *J Light Technol*. 1997;15(8):1263–76.
- [36] Meller SA, de Vries MJ, Arya V, Claus RO, Zabaronick N. Advances in optical fiber sensors for vehicle detection. In *Intelligent Transportation Systems 1998 Jan 27* (Vol. 3207, pp. 318-323). International Society for Optics and Photonics.

- [37] Wang K, Wei Z, Chen B, Cui HL. A fiber-optic weigh-in-motion sensor using fiber Bragg gratings. In *Fiber Optic Sensor Technology and Applications IV* 2005 Nov 10 (Vol. 6004, p. 60040S). International Society for Optics and Photonics.
- [38] Moyo P, Brownjohn JM, Suresh R, Tjin SC. Development of fiber Bragg grating sensors for monitoring civil infrastructure. *Engineering structures*. 2005 Oct 1;27(12):1828-34.
- [39] Berardis S, Caponero MA, Felli F, Rocco F. Use of FBG sensors for weigh in motion. In *17th International Conference on Optical Fibre Sensors* 2005 May 23 (Vol. 5855, pp. 695-699). International Society for Optics and Photonics.
- [40] Casas JR, Cruz PJ. Fiber optic sensors for bridge monitoring. *Journal of bridge engineering*. 2003 Nov;8(6):362-73.
- [41] Udd E, Kunzler M, Laylor HM, Schulz WL, Kreger ST, Coronas JC, McMahon R, Soltész SM, Edgar R. Fiber grating systems for traffic monitoring. In *Health Monitoring and Management of Civil Infrastructure Systems* 2001 Aug 3 (Vol. 4337, pp. 510-517). International Society for Optics and Photonics.
- [42] Mimbela LE, Pate J, Copeland S, Kent PM, Hamrick J. Applications of fiber optics sensors in weigh-in-motion (WIM) systems for monitoring truck weights on pavements and structures. New Mexico. Dept. of Transportation; 2003 Apr 1.
- [43] Oh HS, Sim J. Interface debonding failure in beams strengthened with externally bonded GFRP. *Composite Interfaces*. 2004 Jan 1;11(1):25-42
- [44] Hill KO, Fujii Y, Johnson DC, Kawasaki BS. Photosensitivity in optical fiber waveguides: Application to reflection filter fabrication. *Appl Phys Lett*. 1978;32(10):647-9.

- [45] Zhou Z, Liu W, Huang Y, Wang H, Jianping H, Huang M, et al. Optical fiber Bragg grating sensor assembly for 3D strain monitoring and its case study in highway pavement. *Mech Syst Signal Process.* 2012; 28:36–49.
- [46] Massaroni C, Saccomandi P, Schena E. Medical smart textiles based on fiber optic technology: an overview. *Journal of functional biomaterials.* 2015 Apr 13;6(2):204-21.
- [47] Zhang Z, Huang Y, Palek L, Strommen R. Glass fiber-reinforced polymer-packaged fiber Bragg grating sensors for ultra-thin unbonded concrete overlay monitoring. *Struct Heal Monit .* 2015;14(1):110–23.
- [48] Al-Tarawneh M, Huang Y. Glass fiber-reinforced polymer packaged fiber Bragg grating sensors for low-speed weigh-in-motion measurements. *Opt Eng.* 2016;55(8).
- [49] Bajwa R, Rajagopal R, Varaiya P, Kavalier R, Street N. In-Pavement Wireless Sensor Network for Vehicle Classification. *Proc 10th ACM/IEEE Int Conf Inf Process Sens Networks.* 2011;(August 2016):85–96.
- [50] Udd E, Kunzler M. Development and evaluation of fiber optic sensors. 2003 May.
- [51] Doi S. Non-uniformity Compensation for Fiber Optic Weigh-in-motion Sensor (Doctoral dissertation, Florida Institute of Technology), 2004.
- [52] Hallenbeck ME, Selezneva OI, Quinley R. Verification, Refinement, and Applicability of Long-Term Pavement Performance Vehicle Classification Rules. 2014 Nov.
- [53] Liu J, Sun J, Wang S. Pattern recognition: An overview. *IJCSNS International Journal of Computer Science and Network Security.* 2006 Jun;6(6):57-61.
- [54] Kato T, Ninomiya Y, Masaki I. Preceding Vehicle Recognition Based on Learning from Sample Images. *IEEE Trans Intell Transp Syst.* 2002;3(4):252–9.

- [55] Sun C, Ritchie SG, Oh S. Inductive classifying artificial network for vehicle type categorization. *Computer-Aided Civil and Infrastructure Engineering*. 2003 May 1;18(3):161-72.
- [56] Sroka R. Data Fusion Methods Based on Fuzzy Measures in Vehicle Classification Process. In: *Proceedings of the 21st IEEE Instrumentation and Measurement Technology Conference (IEEE Cat No04CH37510)*. 2004. p. 2234–9.
- [57] Nelson BN. Automatic vehicle detection in infrared imagery using a fuzzy inference-based classification system. *IEEE Trans Fuzzy Syst*. 2001;9(1):53–61.
- [58] Mussa R, Kwigizile V, Selekwa M. Probabilistic Neural Networks Application for Vehicle Classification. *J Transp Eng*. 2006;132(4):293–302.
- [59] Selekwa MF, Kwigizile V, Mussa RN. Setting up a probabilistic neural network for classification of highway vehicles. *International Journal of Computational Intelligence and Applications*. 2005 Dec;5(04):411-23.
- [60] Schölkopf B, Sung KK, Burges CJC, Girosi F, Niyogi P, Poggio T, et al. Comparing support vector machines with gaussian kernels to radial basis function classifiers. *IEEE Trans Signal Process*. 1997;45(11):2758–65.
- [61] Refai H, Naim B, Schettler J, Kalaa OA. The study of vehicle classification equipment with solutions to improve accuracy in Oklahoma. Oklahoma City, OK: Oklahoma Department of Transportation, 2014.; 2014.
- [62] Al-Tarawneh M, Huang Y. In-pavement fiber Bragg grating sensors for high-speed weigh-in-motion measurements. In *Sensors and Smart Structures Technologies for Civil, Mechanical, and Aerospace Systems 2017* 2017 Apr 12 (Vol. 10168, p. 101681Y). International Society for Optics and Photonics.

- [63] Zhang Z, Huang Y, Bridgelall R, Palek L, Strommen R. Sampling optimization for high-speed weigh-in-motion measurements using in-pavement strain-based sensors. *Meas Sci Technol*. 2015;26(6):65003.
- [64] Madevska-Bogdanova A, Nikolik D, Curfs L. Probabilistic SVM outputs for pattern recognition using analytical geometry. *Neurocomputing*. 2004;62(1–4):293–303.
- [65] Burges CJC. A Tutorial on Support Vector Machines for Pattern Recognition. *Data Min Knowl Discov*. 1998;2(2):121–67.
- [66] Chen Z, Pears N, Freeman M, Austin J. Road vehicle classification using Support Vector Machines. *2009 IEEE Int Conf Intell Comput Intell Syst*. 2009;4(1):214–8.
- [67] Kallas M, Francis C, Kanaan L, Merheb D, Honeine P, Amoud H. Multi-class SVM classification combined with kernel PCA feature extraction of ECG signals. In *2012 19th International Conference on Telecommunications (ICT) 2012 Apr 23 (pp. 1-5)*. IEEE.
- [68] Chih-Wei Hsu, Chih-Chung Chang and C-JL. A Practical Guide to Support Vector Classification. *BJU Int*. 2008;101(1):1396–400.
- [69] Kornaropoulos EM, Tsakalides P. A novel KNN classifier for acoustic vehicle classification based on alpha-stable statistical modeling. In *2009 IEEE/SP 15th Workshop on Statistical Signal Processing 2009 Aug 31 (pp. 1-4)*. IEEE.
- [70] Transportation Officials. *AASHTO Guide for Design of Pavement Structures*, 1993. AASHTO; 1993.
- [71] Jiang Y, Li S, Nantung T, Chen H. Analysis and determination of axle load spectra and traffic input for the mechanistic-empirical pavement design guide. *FHWA/IN/JTRP-2008/07*, 2008

- [72] Huang Y. Pavement analysis and design. 2nd ed. Upper Saddle River,NJ: Pearson Prentice Hall; 2004.
- [73] American Association of State Highway and Transportation Officials (AASHTO). Standard Method of Test for Determining Dynamic Modulus of Hot Mix Asphalt (HMA). 2011.
- [74] Rais NM, Wahab MY, Endut IR, Latif AA. Dynamic modulus master curve construction using the modified MEPDG model. In2013 1st International Conference on Artificial Intelligence, Modelling and Simulation 2013 Dec 3 (pp. 212-216). IEEE.
- [75] Scheuter F. Evaluation of factors affecting WIM system accuracy. InProceedings of the Second European Conference on COST 1998 May (Vol. 323, pp. 14-16).